

Atomistic-continuum modeling of short laser pulse melting of Si targetsV. P. Lipp,^{1,2,*} B. Rethfeld,¹ M. E. Garcia,² and D. S. Ivanov^{1,2}¹*Department of Physics and OPTIMAS Research Center, Technical University of Kaiserslautern, Kaiserslautern, Germany*²*Theoretical Physics (FB10), University of Kassel, Kassel, Germany*

(Received 28 July 2014; revised manuscript received 16 November 2014; published 24 December 2014)

We present an atomistic-continuum model to simulate ultrashort-pulse laser melting processes in semiconductor solids on the example of silicon. The kinetics of transient nonequilibrium phase transition mechanisms is addressed with a molecular dynamics method at atomic level, whereas the laser light absorption, strong generated electron-phonon nonequilibrium, fast diffusion of and heat conduction due to photoexcited free carriers are accounted for in the continuum. We give a detailed description of the model, which is then applied to study the mechanism of short laser pulse melting of freestanding Si films. The effect of laser-induced pressure and temperature of the lattice on the melting kinetics is investigated. Two competing melting mechanisms, heterogeneous and homogeneous, were identified. Apart from the classical heterogeneous melting mechanism, the nucleation of the liquid phase homogeneously inside the material significantly contributes to the melting process. The simulations showed, that due to the open diamond structure of the crystal, the laser-generated internal compressive stresses reduce the crystal stability against the homogeneous melting. Consequently, the latter can take a massive character within several picoseconds upon the laser heating. Due to the negative volume of melting of modeled Si material, -7.5% , the material contracts upon the phase transition, relaxes the compressive stresses, and the subsequent melting proceeds heterogeneously until the excess of thermal energy is consumed. The threshold fluence value, at which homogeneous nucleation of liquid starts contributing to the classical heterogeneous propagation of the solid-liquid interface, is found from the series of simulations at different laser input fluences. For the example of Si, the laser melting kinetics of semiconductors was found to be noticeably different from that of metals with a fcc crystal structure.

DOI: [10.1103/PhysRevB.90.245306](https://doi.org/10.1103/PhysRevB.90.245306)

PACS number(s): 79.20.Ds, 02.70.Ns, 31.15.xv, 79.20.Eb

I. INTRODUCTION

Short laser pulse processing of semiconductors has been rapidly progressing during the last several decades. The ability to deposit large amounts of energy into a tightly localized area has found a number of applications in pico- and femtosecond laser machining [1–3] and nanostructuring [4,5] of semiconductors. Specifically, the experiments aimed at semiconductor surface modifications have revealed a particular interest in biotechnology [6] and information technology [7,8]. Nevertheless, while technical progress has a successful tendency of structure production on semiconductor surfaces downscaled to nanometer size [9,10], the fundamental mechanisms behind such laser-induced processes as ultrafast melting, spallation, and ablation are still a subject of active scientific discussion. While the melting time of Si on the order of 10 ns, measured in experiments [11], can be explained with a commonly accepted nucleation theory based on a hydrodynamic model [12], the ultrafast solid-liquid phase transition on the order of a few picoseconds and shorter implies a closer look at the kinetics of microscopic mechanisms of melting at the atomic level. It was shown that under extreme conditions generated in the solids due to femtosecond laser pulse irradiation, ultrafast melting may occur [13]. Also, significant crystal superheating in the presence of strong temperature and pressure gradients influences the melting kinetics.

Moreover, the conditions in the center of the laser spot lead to lateral confinement of the material, so that the excited solid is subjected to one-dimensional expansion toward the surface. This effect may influence the stability of crystal against the melting process [14].

At present, there are a number of modern approaches for the theoretical description of laser-excited semiconductor solids. Details of electron dynamics and the material's reaction can be studied with sophisticated kinetic methods [15–18] and *ab initio* molecular dynamics (MD) approaches [19–23]. Larger ensembles and longer time scales are preferably studied with continuum methods. For instance, hydrodynamic models [24–26] allow for a good precision and are widely accepted among the experimentalists for the obtained data analysis. Due to its low computational cost, relatively simple implementation, and meanwhile ability to account for laser energy absorption, fast electron heat conduction, and strong laser-induced electron-phonon nonequilibrium, the so-called two-temperature model (TTM) [27] has become one of the most famous continuum approaches in ultrashort laser pulse experimental data interpretation and material properties determination [28–33]. The essential problem of the continuum approaches, however, is their assumption of more or less local equilibrium conditions for a description of the laser-induced phase transition processes in the solid such as ultrafast laser melting, spallation, and ablation processes. Together with the strong sensitivity of the hydrodynamic systems to variations in parameters and the usages of phase diagrams and equation of states derived in the assumption of the equilibrium conditions as well, all this limits the validity of such models' applications. This situation becomes even worse specifically under

*v.p.lipp@gmail.com

conditions realized during ultrashort (pico- and femtosecond) laser pulse experiments, where the investigated material is driven to extreme transient states and nonequilibrium phase transition processes become dominant [34]. Noteworthy is that the inclusion of such effects as crystal structure and defects, as well as nonthermal phenomena, into a continuum approach for a microscopic analysis of the femtosecond laser-induced phase transition mechanisms is in general questionable.

Another possible technique to model the response of semiconductor solids to ultrashort laser irradiation is the classical MD. The classical MD is based on the solution of the Newtonian equation of motion for every particle in the system in three-dimensional space using empirical or *ab initio* interatomic potentials. The essential advantage of the MD method is that no assumptions are made regarding the kinetics of nonequilibrium phase transitions at the atomic level. The kinetics of the laser-induced processes therefore follows *a priori* from the interatomic potential only. Specifically, the MD can provide insights into the atomic-level mechanisms of nonequilibrium phase transitions. This method has been demonstrated to be an efficient tool for a microscopic analysis of the melting mechanisms under conditions of overheating in both the bulk of a crystal [35,36] and in systems with free surfaces [37,38]. Simulations of boiling, spinodal decomposition and fragmentation of a metastable liquid [39–41], generation of defects and propagation of laser-induced pressure waves [42,43], and laser ablation [44–48] have also been reported. In the case of Si, the classical MD model, implementing for example such potentials as Stillinger-Weber [49] or modified Tersoff (or MOD) [50], can describe not only the crystal structure, bulk modulus, and cohesive energy, but reproduces very well such important thermophysical properties of Si material as heat capacity, equilibrium melting temperature, and volume of melting. The microscopical analysis of the atomic system in the MD approach results in the availability of the full statistical information and readily allows for the calculation of all macroscopic parameters such as temperature and pressure. Along with modern computational technologies and utilization of the parallel algorithms, the MD approach can cover temporal and spatial scales big enough to be directly attainable in the experiment for a direct comparison with the experiment [51]. All of the above, in essence, justifies the applicability of the MD method in investigation of the kinetics of the ultrashort laser-induced processes in solids and in particular in semiconductors.

The classical MD method, however, is not directly applicable for the simulation of ultrashort laser interactions with semiconductors. For instance, since the electronic contribution to the thermal conductivity of the laser-excited semiconductors is dominant, the conventional MD method, where only a lattice contribution is considered [52], significantly underestimates the total thermal conductivity. This leads to an unphysical confinement of the deposited laser energy in the surface region of the irradiated target. Moreover, the laser energy deposition by multiphoton absorption and a transient state of strong electron-lattice nonequilibrium cannot be reproduced since the electrons are not explicitly presented in the model.

The analysis of the mentioned models suggests that it is possible to consolidate different techniques within a single computational approach. Thus, a model unifying the atomistic description of the kinetics of the laser-induced phase transition processes along with the description of photoexcited free carriers dynamics in the continuum can be constructed for semiconductors (in this work, Si), as it was realized in the atomistic-continuum approach (MD-TTM) for metals [53].

Several similar attempts aiming at the simulation of silicon under the conditions of laser irradiation have been recently undertaken. The TTM-like approaches [54–57] provide many insights into the reaction of the material. However, the detailed kinetics of the material modification may only be obtained with more sophisticated approaches. In Ref. [58] the authors show that the hydrodynamic effects play an important role in the description of the surface modification and ripple formation. At the same time, the kinetic approach [16], though more difficult in the implementation, leads to a deeper understanding of the processes involved, such as the influence of possible local nonequilibrium in an electronic subsystem on the material evolution. In Ref. [59] the authors suggest the atomistic-continuum approach, in which the electronic subsystem is described with a nondegenerate model based on the Boltzmann distribution of the photoexcited carriers. A pioneer work [60] presented a model for the UV laser pulse interaction with semiconductor solids on the example of Si, using a combination of the MD approach (to describe the atomic subsystem) and the Monte Carlo method (for the electrons and holes kinetics, applying the assumption of free carriers). Authors accounted for the changes in the interatomic bonding due to carrier photoexcitation by omitting the attraction part of the interatomic potential. Another work reported in Ref. [61] was aimed at accounting for the changes in the atomic bonding of Si connected to the electron excitation. The corresponding potential depended on the electronic temperature as a parameter and its function was fit to density functional theory simulations of silicon in the assumption that the electrons and holes have common Fermi-Dirac distribution. The authors admit that they do not have a rigorous connection between the electronic states and the interatomic potential, which might lead to imprecise energy conservation [62].

In this work, we develop the atomistic-continuum approach for the modeling of short laser pulse interaction with free-standing Si targets at fluences above the melting threshold. We begin with the description of the continuum approach based on a TTM-like model. As this model includes the equation for the density n of electrons and holes, we will denote it n TTM [57] here and throughout the paper. Then we give the details on the MD approach to model silicon materials and explain the coupling of the MD and n TTM models into the single combined computational approach. Finally, we apply the formulated model for investigation of the kinetics of short laser pulse melting of Si films and discuss the obtained results. In particular, we compare the MD- n TTM model predictions with the results of the continuum approach n TTM alone and with the results of simulations of metal targets. The kinetics of laser melting of Si materials will be studied under different fluences below and above the melting threshold.

II. DESCRIPTION OF THE CONTINUUM APPROACH n TTM

The continuum n TTM approach is based on the model by van Driel [55], in which the solid (silicon) is considered as two coupled subsystems: the phonons and the electron-hole free carriers. Due to laser pulse irradiation (in this work Ti:sapphire laser at 800 nm wavelength), the free carriers are generated, electrons in the conduction band and holes in the valence band, by one- and two-photon absorption processes. Both types of carriers are assumed to quickly equilibrate in the corresponding parabolic bands. To each of them, we apply separate Fermi-Dirac distributions with different chemical potentials, φ_e and φ_h for the electrons and holes respectively, but with a shared carrier density n and temperature T_e [63]. We assume the Dember field prevents charge separation, and consequently the two types of carriers move together. The model accounts for the system of three equations: a continuity equation for free-carrier density and two coupled energy balance equations, one for carriers and one for phonons. Owing to its similarity with an ordinary well-known TTM model [27], but with an additional equation for free-carrier density n , here and later we will refer to this approach as the n TTM model. The model parameters as well as the meaning of symbols can be found in Appendix A. The continuity equation for the density of excited free carriers can be written as [55]

$$\frac{\partial n}{\partial t} + \nabla \cdot \vec{J} = S_n - \gamma n^3 + \delta n, \quad (1)$$

where \vec{J} is the carrier density flux; the first term on the right side, S_n , describes the free-carrier generation rate due to one- and two-photon absorption; the second and third terms account for the processes of Auger recombination and impact ionization, correspondingly.

The balance equation for the free-carrier energy density u can be written as

$$\frac{\partial u}{\partial t} + \nabla \cdot \vec{W} = S_u - \frac{C_{e-h}}{\tau_{ep}}(T_e - T_a), \quad (2)$$

where \vec{W} is the carrier energy flux. It takes into account the carrier thermal conductivity as well as the energy transfer due to the carrier flux. The first term on the right side, S_u , describes the energy absorption processes: free-carrier energy gain, and one- and two-photon absorption. The last term accounts for the electron-phonon energy exchange between free carriers with temperature T_e and phonons with temperature T_a . This term strongly depends not only on the electron-phonon temperature difference, but also on the heat capacity of free carriers C_{e-h} and electron-phonon relaxation time τ_{ep} , which in general are functions of free-carrier temperature and density. The energy balance equation for the phonon subsystem therefore is written as follows:

$$C_a \frac{\partial T_a}{\partial t} = \nabla \cdot (k_a \nabla T_a) + \frac{C_{e-h}}{\tau_{ep}}(T_e - T_a). \quad (3)$$

The first term on the right side accounts for the phonon conduction process, which in practice—due to small phonon conductivity k_a —is negligible and frequently omitted. The electron-phonon energy exchange term is dominant here.

Special attention must be paid here to the source terms describing both the rate of free-carrier density growth and the corresponding process of their energy increase, taking place in Eqs. (1) and (2), correspondingly, and given by

$$S_n = \frac{\alpha I_{\text{abs}}(\vec{r}, t)}{\hbar\omega} + \frac{\beta I_{\text{abs}}^2(\vec{r}, t)}{2\hbar\omega}, \quad (4)$$

$$S_u = \alpha I_{\text{abs}}(\vec{r}, t) + \beta I_{\text{abs}}^2(\vec{r}, t) + \Theta n I_{\text{abs}}(\vec{r}, t). \quad (5)$$

For ultrashort laser material interactions, a one-dimensional heating problem is often analyzed in the case of the heating spot size being much larger than the size of the thermally affected zone, analyzed in the modeling. The corresponding form of laser intensity at the surface ($z = 0$) in this case is

$$I_{\text{abs}}(0, t) = [1 - R(T_a)] \sqrt{\frac{\nu}{\pi}} \frac{\Phi_{\text{inc}}}{t_p} e^{-\nu[(t-3t_p)/t_p]^2}, \quad (6)$$

where Φ_{inc} is the incident fluence, $\nu = 4 \ln 2$, and $R(T_a)$ is the reflectivity function. In this work, to prescribe the demanded incident fluence, the center of the Gaussian pulse is shifted from the initial time $t = 0$ to 3 pulse duration times t_p , that in turn is defined at the full width at half maximum.

The spatial dependence of I_{abs} can be found upon the solution of the differential equation of the attenuation process:

$$\frac{dI_{\text{abs}}(z, t)}{dz} = -\alpha I_{\text{abs}}(z, t) - \beta I_{\text{abs}}^2(z, t) - \Theta n I_{\text{abs}}(z, t), \quad (7)$$

where z is the depth into the sample; the terms on the right side are responsible for one- and two-photon absorption, and for the free-carrier absorption processes correspondingly. According to this equation, the spatial attenuation of the laser strongly depends on the transient electron density and therefore may strongly change during the pulse.

Finally, the expression for the total energy density of free carriers (consisting of potential and kinetic parts) closes the comprised system of equations (1)–(3) and is given by

$$u = n E_g(n, T_a) + \frac{3}{2} n k_B T_e [H_{1/2}^{3/2}(\eta_e) + H_{1/2}^{3/2}(\eta_h)], \quad (8)$$

where k_B is the Boltzmann constant, E_g is the band gap, and $H_y^x(\eta_c)$ are the functions described in Appendix B. This Appendix also includes the constitutive expressions (B5) and (B7) for \vec{J} and \vec{W} demanded for the system solution. Here we only show the equations needed to understand the general idea of the approach.

The system of equations (1)–(3) is written in the conservative form, which provides the exact energy conservation in the case of numerical solution. Nevertheless it is not convenient to solve, since Eq. (2) includes both T_e and u . One can rewrite Eq. (2) using variables n , T_a , and T_e for a more handy numerical form. To do so, we have to note that the specific heat capacity of the carriers is $C_{e-h} = \partial u / \partial T_e|_n$, and using Eq. (8) we can therefore write

$$C_{e-h} = \frac{3}{2} n k_B \left\{ H_{1/2}^{3/2}(\eta_e) + H_{1/2}^{3/2}(\eta_h) + T_e \frac{\partial \eta_e}{\partial T_e} [1 - H_{1/2}^{3/2}(\eta_e) H_{1/2}^{-1/2}(\eta_e)] + T_e \frac{\partial \eta_h}{\partial T_e} [1 - H_{1/2}^{3/2}(\eta_h) H_{1/2}^{-1/2}(\eta_h)] \right\}. \quad (9)$$

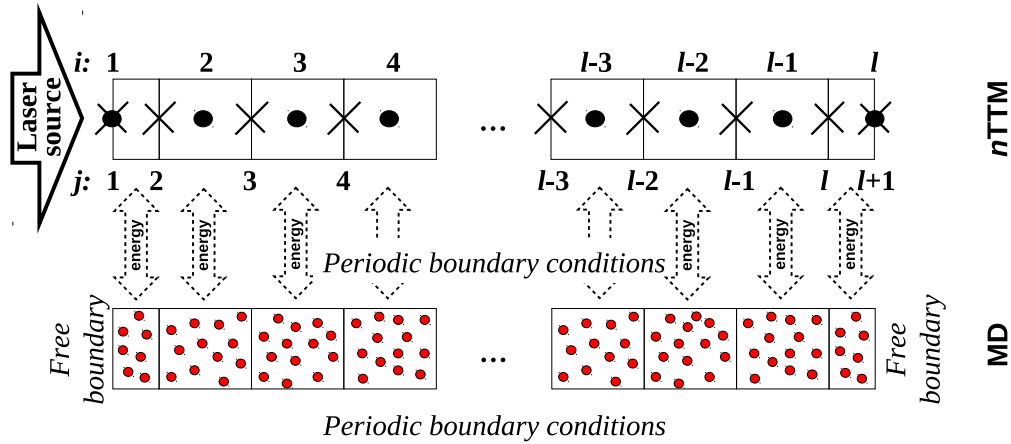


FIG. 1. (Color online) The finite-difference grid mesh of the n TTM model and the organization of the coupling between the n TTM and MD models. Symbol “•” indicates the grid points for n , T_e , and T_a ($i = 1, 2, \dots, l$); symbol “×” indicates the grid points for J , W , $k_a \frac{\partial T_a}{\partial z}$, and E_g ($j = 1, 2, \dots, l + 1$). Red circles represent atoms.

Calculating $\partial u / \partial t$ from Eq. (8) and substituting it to Eq. (2) we arrive at the diffusionlike equation for the temperature of electron-hole pairs:

$$\begin{aligned}
 C_{e-h} \frac{\partial T_e}{\partial t} = & S_u - \nabla \cdot \vec{W} - \frac{C_{e-h}}{\tau_{ep}} (T_e - T_a) \\
 & - \frac{\partial n}{\partial t} \left\{ E_g + \frac{3}{2} k_B T_e [H_{1/2}^{3/2}(\eta_e) + H_{1/2}^{3/2}(\eta_h)] \right\} \\
 & - n \left(\frac{\partial E_g}{\partial n} \frac{\partial n}{\partial t} + \frac{\partial E_g}{\partial T_a} \frac{\partial T_a}{\partial t} \right) \\
 & - \frac{3}{2} k_B T_e n \frac{\partial n}{\partial t} \left\{ [1 - H_{1/2}^{3/2}(\eta_e) H_{1/2}^{-1/2}(\eta_e)] \frac{\partial \eta_e}{\partial n} \right. \\
 & \left. + [1 - H_{1/2}^{3/2}(\eta_h) H_{1/2}^{-1/2}(\eta_h)] \frac{\partial \eta_h}{\partial n} \right\}. \quad (10)
 \end{aligned}$$

As opposite to Eq. (2), Eq. (10) may lead to the accumulation of numerical errors in the case of low precision of the derivative calculations of the last three terms, i.e., it is written in the nonconservative form. The errors may come from the last terms of Eq. (10), which numerically play a role of extra sources in the diffusion equation. Nevertheless our semi-implicit numerical scheme provides the precision, which is more than enough for our purposes. The details of the continuum approach described above and the derivation of the main equations can be found in Ref. [55].

Thus, from the system of equations (1), (3), and (10), we can fully determine the dynamics of n , T_e , and T_a in one dimension (1D) with the following initial and boundary conditions, suitable for a freestanding film:

$$\begin{aligned}
 T_a(z, 0) = T_e(z, 0) = & 300 \text{ K}, \\
 n(z, 0) = n_{\text{eq}} = & 10^{16} \text{ m}^{-3}, \quad \text{Ref. [64]}, \\
 J(0, t) = J(L, t) = & 0, \\
 W(0, t) = W(L, t) = & 0, \\
 k_a \frac{\partial T_a}{\partial z}(0, t) = k_a \frac{\partial T_a}{\partial z}(L, t) = & 0,
 \end{aligned} \quad (11)$$

where L is the thickness of the sample.

To solve the above system, we use the finite-difference grid mesh sketched in Fig. 1 (upper part). The sample is divided into cells according to the scheme, and the thermodynamic parameters are calculated in each cell. The spatial derivatives of n , T_e , T_a , J , W , $k_a \frac{\partial T_a}{\partial z}$, and E_g at the interior points are approximated with the central difference, and those at the boundary are evaluated with the first-order approximation.

During the solution of the considered system of equations we use a semi-implicit Crank-Nicolson numerical scheme [65,66] modified for this nonlinear case with the predictor-corrector algorithm. The details of the integration algorithm will be published elsewhere [67]. This approach allowed us to increase the time step of the calculations from 10^{-20} s up to 10^{-16} s as compared to the explicit scheme with an energy conservation error of less than 0.2%. Thus, the time step of 10^{-17} s still lets the system be solved fast enough with nearly perfect energy conservation.

When being combined with MD, the proposed implicit scheme of the n TTM model solution gives a significant benefit. Since its relative calculation time is significantly shorter than that for the MD part, the inclusion of n TTM in MD will not influence the calculation time of the combined model.

One of the most uncertain parameters in the n TTM model is the two-photon absorption coefficient. For our wavelength (800 nm), the experimental measurements in Ref. [68] yield the value of $\beta = 2$ cm/GW, while fitting to another experiment [69] gives $\beta = 55$ cm/GW. If a continuum model is involved in fitting [54], one has the value of $\beta = 9$ cm/GW. Since this parameter plays an important role in laser absorption, it noticeably influences the amount of energy absorbed in and transmitted through the sample. Our simulations show a large difference in the absorbed fluence when using different values of the β parameter. In the presented productive runs, the value of $\beta = 15$ cm/GW was chosen for calculations. This choice is justified by a good agreement between the experimental melting threshold found for the 130 fs laser pulse [70–72] (0.26 – 0.27 J/cm²), the one predicted from n TTM (0.29 J/cm² in our calculations), and the one obtained from the combined model (0.27 J/cm²; see below). Also, in our present calculations we used a constant

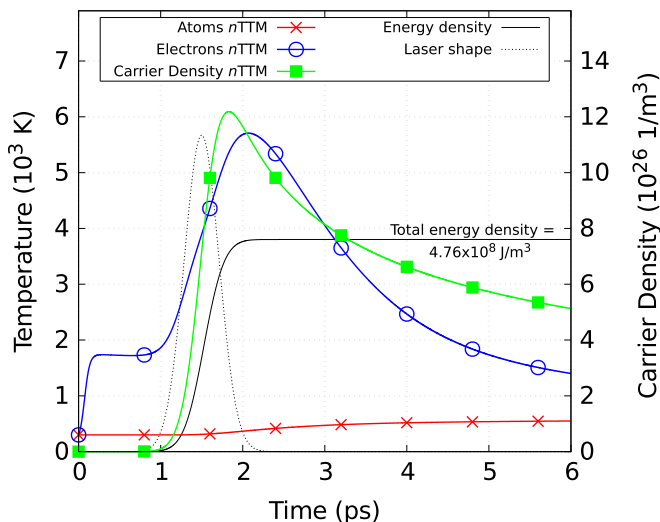


FIG. 2. (Color online) Carrier/lattice temperatures and carrier density dynamics on the sample surface according to the n TTM model followed by the 500 fs laser pulse at the absorbed fluence of 0.0381 J/cm^2 . The sample thickness is 800 nm. The laser pulse shape and the energy density, proving energy conservation, are not in scale.

value of γ for the Auger recombination coefficient. However, according to [73], accounting for the effect of nondegeneracy at high carrier densities, as is done in Ref. [54], leads to a different characteristic time of the free-carrier recombination. Additionally, in Ref. [57] the authors suggested an extension to the model of van Driel, based on the Drude model. It accounts for the changes in the optical parameters, namely, reflectivity and free-carrier absorption coefficient, due to the highly transient free-carrier density during the excitation with femtosecond laser pulses. These modifications are therefore planned for implementation in our future research.

As an example of n TTM model application, in Fig. 2 we show the electron-hole density and temperature as well as atomic temperature dynamics on the surface, followed by the laser pulse irradiation of 500 fs duration at the absorbed fluence of 0.0381 J/cm^2 (corresponding to the incident fluence of 0.15 J/cm^2 via the reflectivity function used in the model [74]). The Si sample thickness was taken to be 800 nm. The initial increase in the number of free carriers, followed by the laser pulse, changes to its decay due to Auger recombination and diffusion processes. Interestingly, the electron-hole temperature exhibits two elevations. The first one is associated with a very low density of free carriers, which consequently have negligible heat capacity (9) and possess very little energy. The subsequent plateau corresponds to the temporal prevalence of one-photon absorption over all other processes, so that all created free electron-hole pairs fall into the same energy level $u/n = \hbar\omega$. The second increase of the temperature is connected to the free-carrier absorption and its following dynamics is pretty much the same as it is for metals given by ordinary TTM [27]. Finally, the thermal energy from hot electron-hole carriers goes to the atomic subsystem of the sample leading to its gradual temperature increase upon the electron-phonon equilibration.

Similar simulations were also performed in Ref. [75]. The comparison of the corresponding solutions, however, shows a significant difference in the carrier's properties dynamics even for the same sample geometry and set of parameters. The essential reason for this discrepancy unfortunately originates from a major mathematical mistake during the derivation of the corresponding equation for the free-carrier's temperature, specifically in Eqs. (18) and (19) of Ref. [75]. As a result, the energy conservation criterion is not fulfilled there.

III. MD APPROACH

One of the main disadvantages of the n TTM model is that it is barely applicable for the description of the kinetics of considered phase transition processes in the continuum. Despite the fact that some of its problems can be solved by means of more sophisticated implementation, the induced phase transformation mechanisms, realized in the solid due to the ultrashort pulse laser irradiation, can be quite far from the equilibrium conditions. The transition times can be shorter than 1 ps and the new phase nuclei may have sizes of several interatomic distances only. Thus, the investigation of such processes as ultrafast melting, ablation, spallation, recrystallization, and surface effects, would require a number of assumptions to be implemented within the n TTM model. We overcome this problem by introducing the atomistic description of the solid with a classical MD method, which will eventually substitute Eq. (3) in the continuum n TTM model. The MD approach is based on the solution of Newtonian equations for every atom [76]. With initial conditions (initial coordinates and velocities of all atoms), the full set of equations in three dimensions (3D) allows for monitoring the microscopic evolution of the system in time. This microscopic information about the system enables us to calculate any macroscopic (thermodynamic) parameters.

As we already mentioned, the choice of the interatomic potential fully determines the kinetics of laser melting and the properties of the material. For our purposes, some potentials are not suitable due to an imprecise representation of thermophysical material properties. For example, the Tersoff potential [77], although well representing the elastic properties, fails in describing the melting temperature and the volume of melting [78]. Analogously, the modified-embedded-atom method [79] is suitable for many materials, but in silicon it leads to an expansion coefficient significantly differing from the experimental value as well as to a noticeably shifted melting point [80]. Consequently, with these potentials, one can expect significantly different melting kinetics as compared with experimental results. In general, the choice of the potential is made upon performing a balance between the simplicity of implementation, computational costs, and the description of important parameters. In the presented work, the interatomic interaction is described via a well-known Stillinger-Weber potential [49]:

$$V = \sum_{\substack{i,j \\ i < j}} U_2(r_{ij}) + \sum_{\substack{i,j,k \\ i < j < k}} U_3(r_{ijk}), \quad (12)$$

where U_2 is the two-body part and U_3 is the three-body part. Provided that the reduced radius $r = \frac{r_{ij}}{\sigma}$ is less than the cutoff

distance a ,

$$U_2 = \varepsilon A (B r^{-p} - 1) e^{(r-a)^{-1}}, \quad (13)$$

$$U_3 = h(r_{ij}, r_{ik}, \theta_{jik}) + h(r_{ji}, r_{jk}, \theta_{ijk}) + h(r_{ki}, r_{kj}, \theta_{ikj}), \quad (14)$$

and zero otherwise. The functions h are given by

$$h(r_{ij}, r_{ik}, \theta_{jik}) = \lambda \exp[\gamma(r_{ij} - a)^{-1} + \gamma(r_{ik} - a)^{-1}] \\ \times (\cos \theta_{jik} + \frac{1}{3})^2, \quad (15)$$

where θ_{jik} is the angle between \vec{r}_j and \vec{r}_k adjoining vectors at vertex i , etc. This dependence on θ_{jik} leads to the crystal with an ideal tetrahedral angle, described with $\cos \theta_{jik} = -1/3$. Thus, the potential describes the open diamond structure of silicon solid. All the parameters in Eqs. (13) and (15), which are fitted to reproduce the properties of silicon crystal, can be found in the original paper [49].

The important thermophysical properties of the modeled silicon such as melting temperature [81], solidification and melting rates [82], thermal conductivity [83,84], bulk modulus [85], and phase diagram [60,86] reproduce the behavior of a real solid at the equilibrium conditions quite well. Moreover, the chosen potential gives a better overall description of liquid phase than all frequently used potentials [85]. Appendix C presents some other important physical properties of Stillinger-Weber potential, which we will need in order to describe the melting kinetics quantitatively. However, it is known that at strong photoexcitation of semiconductors, the changes in electronic density and band structure may lead to a reconstruction of the interatomic bonding and consequently to nonthermal melting [87]. The Stillinger-Weber potential does not account for this behavior; therefore, in the combined model, we restrict ourselves to incident laser fluences below the nonthermal melting threshold, which was determined to be about 0.55 J/cm² for our laser parameters [54]. In our future works we are planning to introduce the modified potential, which will be able to account for the nonthermal effects as well [62].

As was mentioned above, though MD is a powerful tool for the description of solids, it lacks the free electrons in its classical formulation, necessary for description of the laser light absorption, free-carrier diffusion, fast electron heat conduction, and the electron-phonon energy exchange. For the description of free-carrier subsystem dynamics of silicon solid, one can incorporate the described n TTM part into the MD method in a similar manner as was done in Ref. [53]. In other words, we replace Eq. (3) in the n TTM approach with the set of Newtonian equations for each atom in the computational cell, introducing therefore the microscopic approach with all the advantages of both MD and n TTM. The combined MD- n TTM approach, therefore, will provide us with an accurate model for the description of the laser-excited semiconductor solids. The details about organization of the connection between the MD and n TTM parts are described in the following section.

IV. THE COMBINED MD- n TTM MODEL

In this section we explain the organization of the coupling between the continuum and atomistic parts in the combined

MD- n TTM model. The atomic subsystem in the MD part is divided into a number of volume cells (Fig. 1, lower part). Each of them corresponds to the same space geometry in the continuum n TTM part describing the electronic subsystem. In every MD cell we assume local equilibrium and calculate the temperature of atoms under the assumption of equipartition between the kinetic and potential energies, based on the virial theorem:

$$T_a = \frac{2}{3k_B N_c} \sum_{i=1}^{N_c} \frac{m_i (\vec{v}_i)^2}{2}, \quad (16)$$

where N_c is the number of atoms in a given cell c , and \vec{v}_i is the velocity of atom i . The total number of atoms N_c in each cell is defined from two constraints. First, calculating the atomic temperature, we assume the applicability of thermodynamics inside each cell. It means $N_c \gg 1$. The finite value of N_c leads to atomic temperature fluctuations, which decay as $\frac{1}{\sqrt{N_c}}$. Therefore, to prevent the fluctuations one needs a large enough number of atoms in a cell. On the other hand, a smaller number of atoms in a cell (larger number of cells) increases spatial resolution in our carrier dynamics calculations. Thus, the system is organized in such the way that N_c is around 1800 (160 calculation cells), so that the local temperature is reasonably defined and at the same time a sufficient spatial resolution is ensured. In practice, however, test calculations showed no difference between $N_c = 450$ and $N_c = 3600$. In the case of an explicit continuum scheme, the choice of computational cells would also influence the time step of n TTM in a way that bigger cells lead to decreasing the computational costs.

If the material expands (shrinks) during the simulation, we add (delete) a corresponding continuum computational cell. The criterion for the creation (deactivation) of a cell is that the atomic density exceeds (drops down to) the threshold of 10% of the initial average density in the system. The atoms inside the deactivated cells are included in the nearest active cell if they are located within a distance of half-cell size from the active cell. Herewith, all the physical properties of the electronic subsystem such as diffusivity and thermal conductivity, the absorption and recombination coefficients, and the electron density are scaled with the relative changes in the atomic density within each cell c , ρ_c/ρ_0 , where ρ_c is the current atomic density in the cell and ρ_0 is the initial atomic density (averaged through the whole atomic system).

Because of the relatively high computational cost of the MD method, we decrease the needed amount of material by modeling a comparatively large laser spot size. This assumption enables us to use a 1D diffusion model in the continuum part and suggests the MD configuration as a thin and long sample, which is hypothetically located at the center of a wide laser spot along the laser pulse propagation. Therefore one can safely apply periodic boundary conditions in the lateral sides of the sample and free boundaries at its front/rear surfaces. In this work all simulations are performed for a sample with $5 \times 5 \times 1472$ crystal cells (294 400 atoms) with the lattice parameter of 0.543 74 nm (for 300 K), which is equivalent to dimensions of $2.72 \times 2.72 \times 800.4$ nm in X , Y , and Z axes, respectively. The lateral sizes (2.72 nm) are chosen so that they are bigger than the characteristic size of liquid nuclei (~ 1 nm) in order to

allow the nuclei to grow. This allows us to describe the kinetics of homogeneous melting. The described computational setup therefore is modeling a freestanding 800 nm Si film. Before the productive simulations, the sample was equilibrated at normal conditions (300 K and at $P = 0$ GPa).

The time steps of MD and continuum parts are synchronized so that $\Delta t_{MD} = k \Delta t_{nTTM}$, where k is an integer number. In our case $\Delta t_{MD} = 0.5 \times 10^{-15}$ s and $k = 50$. This means, while the continuum part is under calculation, the MD part is waiting for the resulting energy, taken away from hot (or coming to cold) electrons accumulated over k steps. As a method to account for the influence of electrons on the atomic motion we include the “friction” term in Newtonian equations of motion for every atom i [53]:

$$m_i \frac{d^2 \vec{r}_i}{dt^2} = \vec{F}_i + \xi m_i \vec{v}_i^T \quad (17)$$

with

$$\xi = \frac{\frac{1}{k} \sum_{j=1}^k G V_c (T_e^j - T_a)}{\sum_i m_i (\vec{v}_i^T)^2}, \quad (18)$$

where $G = C_{e-h}/\tau_{ep}$ stands for the electron-phonon coupling coefficient, and V_c is the volume of the corresponding MD cell. \vec{v}_i^T corresponds to the thermal part of the atomic velocity of atom i after the subtraction of the velocity of center of mass \vec{U}_c of a given cell, $\vec{v}_i^T = \vec{v}_i - \vec{U}_c$. The coefficient ξ is calculated in the same manner as was done in Ref. [53] based on the energy conservation law. It describes the electron-phonon interaction process so that the energy added to (or removed from) each cell of the MD system at each integration MD step would match the energy transferred between the electrons and the lattice during k steps of the finite-difference integration in the continuum part. This “friction approach” is chosen due to its simplicity in the implementation. We are aware of other ways of adding/removing the energy to/from the atoms (for example, Langevin thermostat [88–90]). Macroscopically we do not expect noticeable differences, because the friction force applied here has random directions originated from the established Maxwellian distribution in randomly oriented atomic velocities. In the following section we present the results of the combined MD- n TTM model for the investigation of short laser pulse melting of freestanding Si film.

V. RESULTS AND DISCUSSIONS

A. Comparison of the n TTM and the combined MD- n TTM models predictions

In order to demonstrate the feasibility of the developed atomistic-continuum model implementation and its applicability in our research, we repeat the modeling of the 500 fs laser pulse interaction with 800 nm freestanding Si film with the combined MD- n TTM model at the absorbed fluence of 0.0381 J/cm². Similar to the result of the n TTM model alone, as is reflected in Fig. 2, the lattice temperature dynamics and the temperature/density of the electron-hole free carriers are shown in Fig. 3 for the front surface cell. As one can see, the combined MD- n TTM model shows no qualitative differences with the continuum calculations. In other words,

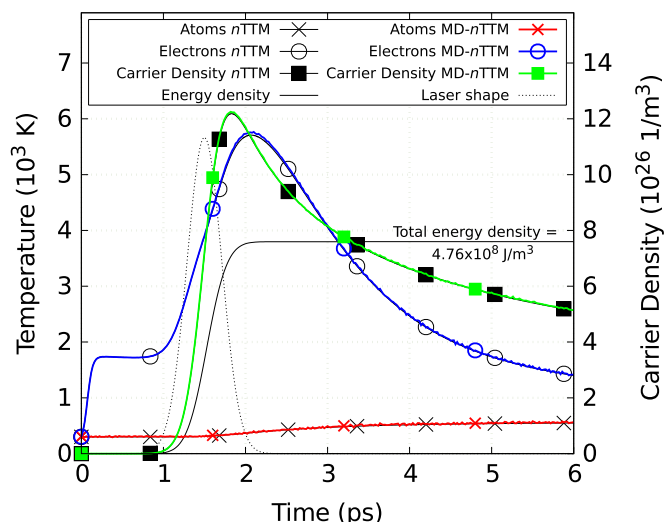


FIG. 3. (Color online) The dynamics of n , T_e , and T_a on the sample surface obtained with n TTM and MD- n TTM models at the same conditions as indicated in Fig. 2: 800 nm sample thickness, 0.0381 J/cm² absorbed fluence, 500 fs pulse duration. The laser pulse shape and energy conservation are shown out of scale.

it describes the absorption of the laser light, fast electron heat conduction, free-carrier diffusion, the laser-generated strong electron-phonon nonequilibrium, and at the same time contains the atomic description of the matter within the frames of a single computational approach. A minor quantitative difference in the surface temperature of atoms, $\sim 3\%$ (apart from the atomic temperature fluctuations, which are natural for a finite amount of atoms), between the predictions by the n TTM and MD- n TTM models, we attribute to the sample expansion process and pressure dynamics, not included into the continuum calculations. This difference is not so pronounced as in the case of metals [91], due to the lower expansion coefficient for silicon (see Table I). The most important benefit of the combined model, however, and eventually the reward for all our efforts is that—in contrast to the continuum calculations given by the n TTM approach—the combined model is now able to distinguish the whole complexity of the kinetics of laser-induced transient processes with atomic precision. This makes the MD- n TTM model a powerful tool in studying the microscopic mechanism of short laser pulse nonequilibrium phase transformations processes that will be discussed in detail below. As a means to control the accuracy of our calculations we apply the energy conservation law. For the combined atomistic-continuum MD- n TTM model the resulting error in energy conservation was found to be less than 0.45% per simulation, which we accept as a good result fulfilling our demands. The comparison of the combined MD- n TTM approach with the n TTM continuum method together with the energy conservation criterion fulfillment, therefore, confirms the accuracy of the constructed model and its applicability in our research.

B. Kinetics of short pulse laser melting of Si

The above developed MD- n TTM approach is applied here to study the kinetics of short laser pulse melting of freestanding

Si films. The parameters of the following simulation were taken according to the experiment [70]: 130 fs laser duration, 0.42 J/cm^2 incident fluence (0.209 J/cm^2 absorbed fluence given by the used reflectivity model), and 800 nm laser wavelength. The sample thickness was taken to be 800 nm. From our test simulations we found that this value already represents a thick sample, since no noticeable quantitative or qualitative differences in melting kinetics are present with respect to the targets of 450 and 2000 nm thicknesses. The details of the kinetics of the melting process can be extracted from the sequence of the following contour plots and atomic snapshots. Figure 4(a) represents the contour plot of the percentage of molten material (calculated as the number of “molten atoms” in a cell related to the total number of atoms in it). One atom is considered as “molten” if its central symmetry parameter is lower than a threshold value of 0.9825 (see Appendix D). Figure 4(a) allows one to observe the liquid nuclei generation and their growth in time. The position of the melting front was mapped by the local volumes where 50% of the material is molten. The corresponding melting front curve is shown with a black solid line and, for convenience, replotted on the other contour plots, Figs. 4(b) and 4(c), which show the contour plots of temperature and pressure evolution, respectively. The white frames (rectangles) on the plot in Fig. 4(a) represent the places of the corresponding snapshot series, Figs. 5–7, and are numbered correspondingly. These snapshots are taken at different moments of time after the laser pulse and at different depths. In Figs. 5–7 every point represents an atom. Colors of atoms reflect the local structure according to the central symmetry parameter: The atoms having a crystal surrounding are shown in blue, whereas those submerged in liquid ambient are shown in red. The values of the central symmetry parameter for certain depths are shown for each particle at the figures below the atomic structure.

Upon the laser pulse absorption, the generated strong electron-phonon nonequilibrium leads to the electron-phonon energy exchange, which in turn causes the elevation of the atomic temperature to $T > T_m$ ($T_m = 1683 \text{ K}$; see Appendix C) up to the depth of $\sim 250 \text{ nm}$ within $\sim 4 \text{ ps}$ [Fig. 4(b); in order to provide a better view, the plot only shows 210 nm from the top of the sample]. Before the onset of melting, however, the strong heating rate results in the increase of the pressure [see Fig. 4(c)]. As discussed in Appendix C [see Fig. 11(a)], due to the different slope of the melting curve from that in metals [92], higher pressure reduces the temperature needed to melt the crystal (by both homogeneous and heterogeneous mechanisms) and therefore speeds up the melting process. In the first picoseconds, the sample has a slightly lower pressure near the surface at a higher temperature and a slightly higher pressure in the depth (up to $\sim 100 \text{ nm}$) at a lower temperature. This results in the onset of homogeneous melting taking place simultaneously from the surface up to the depth of $\sim 100 \text{ nm}$ within 4 ps. Notably, the melting speed at this point is much higher than the speed of sound. The significant excess of thermal energy cannot convert the solid into the liquid state by means of a classical heterogeneous solid-liquid interface propagation, and the homogeneous melting mechanism takes a massive character, Fig. 4(a), rectangle 5, and the corresponding

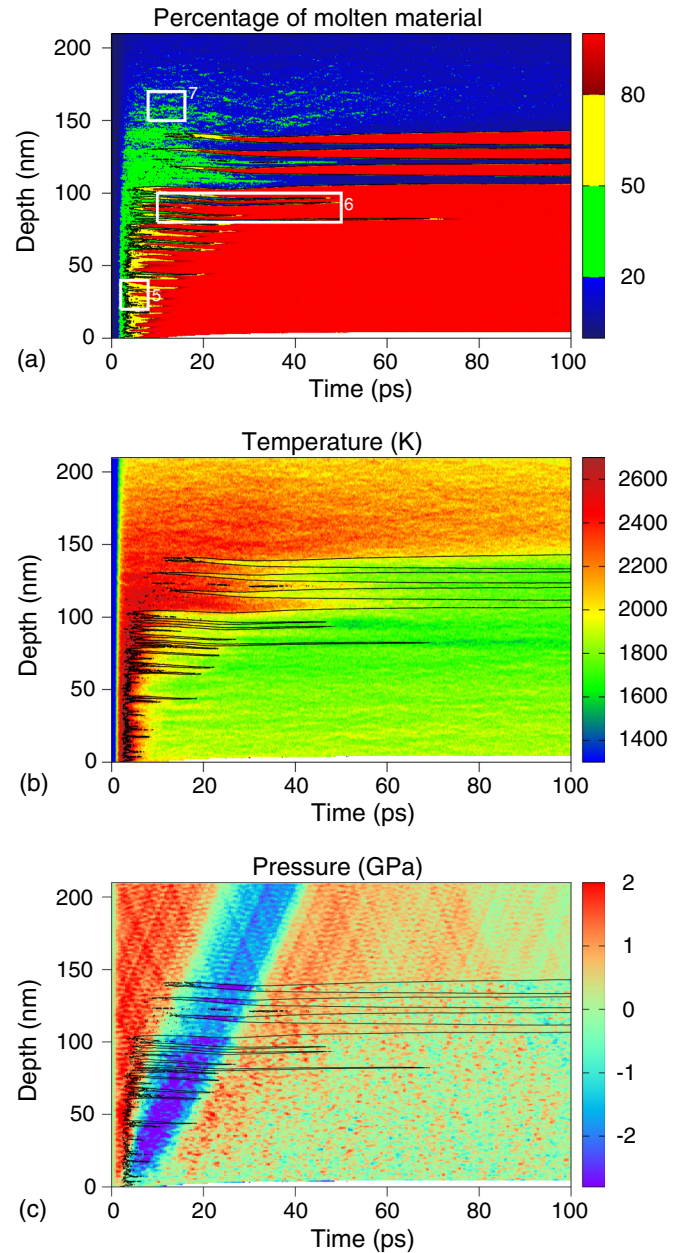


FIG. 4. (Color online) Contour plots of (a) percentage of molten material (according to the central symmetry parameter; see Appendix D), (b) atomic temperature, and (c) atomic pressure, obtained from the simulation of 130 fs laser pulse focused on 800 nm silicon film at the absorbed fluence 0.209 J/cm^2 . The rectangles on the plot (a) show the corresponding positions of the atomic configuration snapshots presented in Figs. 5–7. The black solid line shows the position of the melting front assuming 50% of the material is molten. For a closer look we show the sample depth only up to 210 nm, where the phase transition processes are taking place.

snapshot series in Fig. 5. Such a phenomenon has been already suggested in theoretical work [93].

Here we can see a major difference in the melting process from that observed for metals [94] (which experience expansion upon melting by 3%–5% [95]). In Fig. 4(c), we notice

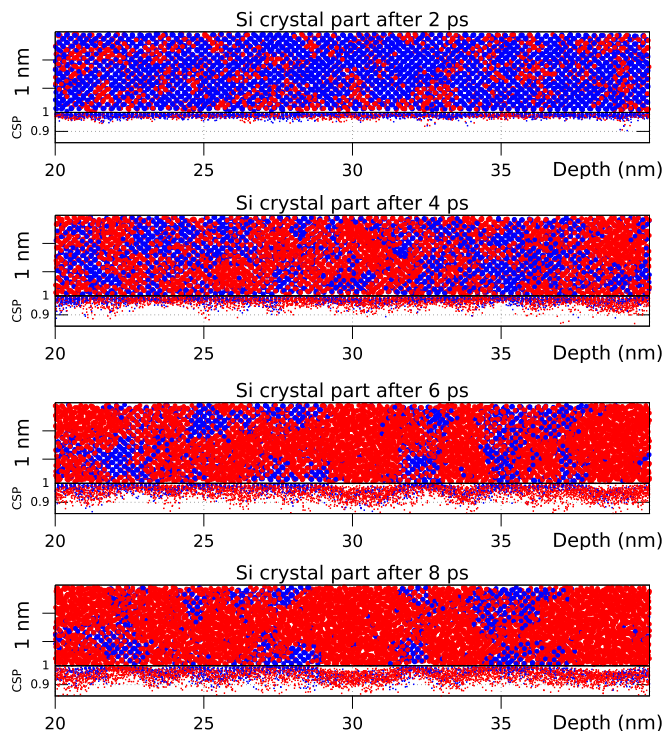


FIG. 5. (Color online) The snapshots of the simulation taken at different moments of time after the laser pulse (130 fs duration, 0.209 J/cm² absorbed fluence) at the depth of 20–40 nm [see rectangle 5 in Fig. 4(a)]. The original laser pulse was directed from the left to the right. According to the central symmetry parameter (shown below each snapshot), the atoms with crystalline surrounding are shown in blue and those submerged in liquid ambient are shown in red. This series shows the presence of only the homogeneous melting mechanism at this depth.

that the initial laser-induced internal compressive stresses are relaxed not by the propagation of the pressure wave across the sample, but essentially by the melting process itself. From the properties of the represented material and Fig. 12(a), we understand it by the fact that the melting process leads to the material volume contraction by approximately 7.5% (see Appendix C), which results in the pressure drop. Consequently, the propagating of an unloading wave decreases the pressure of the remaining solid chunks of the material, which in turn reinforces their stability against the melting process. This is reflected in the abruptly irregular curve of the melting front [Fig. 4(a)]. Upon the relaxation of the tensile stresses via the propagation of the pressure waves, most of the remaining solid chunks lose their stability and the melting immediately finishes. It is reflected as the disappearance of the yellow color in Fig. 4(a). At the places where the temperature is not large enough, the melting proceeds further by the classical heterogeneous mechanism at a much lower rate, which can be seen by rectangle 6 in Fig. 4(a) and in the corresponding snapshots, Fig. 6. Finally, rectangle 7 in Fig. 4(a) and the corresponding snapshot series in Fig. 7 indicate the areas where the temperature-pressure interplay

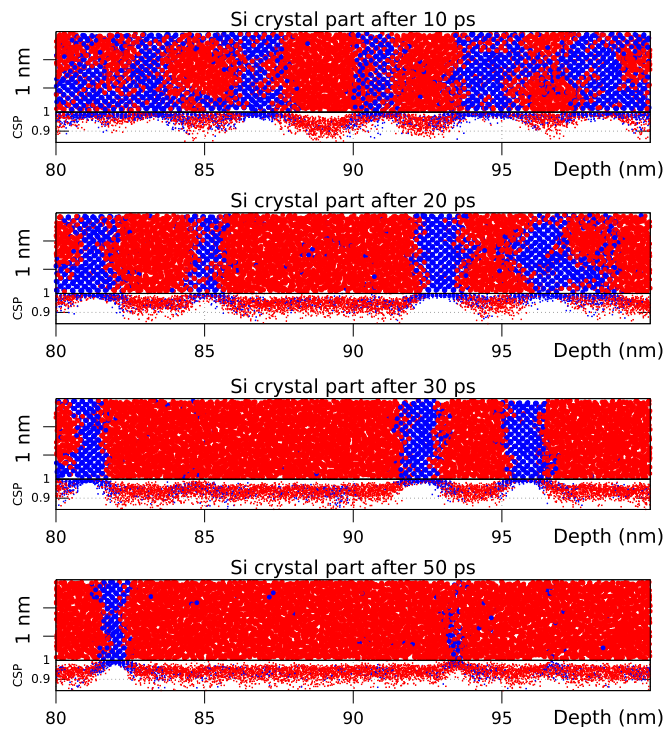


FIG. 6. (Color online) The snapshots of the simulation taken at different moments of time at the depths of 80–100 nm. This is the same simulation and style as in Fig. 5, but refers to rectangle 6 in Fig. 4(a). The series shows the presence of both homogeneous and heterogeneous melting mechanisms at this depth.

mechanism did not result in the onset of either a homogeneous or a heterogeneous melting process. There, the process of new phase nuclei generation can be seen as noise consisting of small molten nuclei. None of them, however, will eventually

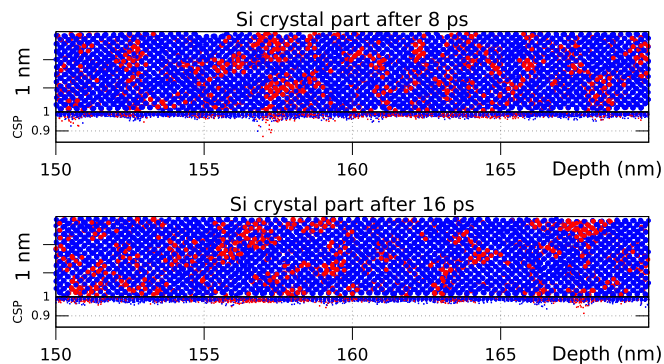


FIG. 7. (Color online) The snapshots taken at different moments of time at the depths of 150–170 nm. This is the same simulation and style as in Fig. 5, but refers to rectangle 7 in Fig. 4(a). The series shows the generation of liquid nuclei that randomly appear and disappear. Under the realized conditions at this depth, however, the liquid nuclei do not grow, which preserves this part of the solid from the onset of melting.

exceed the critical size for the onset of a solid-liquid transition process.

Later (around 200 ps after the laser pulse; not shown), the mentioned negative pressure wave, originated from the material shrinkage, is reflected from the rear surface and returns to the front surface as a compressive wave. This decreases the stability of the lattice and therefore temporarily speeds up the front propagation. See also Sec. VC and Fig. 10 for more details.

For comparison, in Fig. 8 we show the contour plots for another simulation with a smaller absorbed fluence, namely, 0.161 J/cm^2 (corresponding to the incident fluence of 0.34 J/cm^2 via the reflectivity function used in the model). All other conditions in this simulation are the same as before. Figure 8(a) shows the contour plot of the molten material percentage (it is shown with a different scale, compared to the other contour plots, in order to provide a better view). In contrast to the result of the higher fluence simulations, in this case the melting process is fully heterogeneous. Figure 9 shows the corresponding snapshots with a well-defined solid-liquid interface. Despite the fact that the atomic temperature [Fig. 8(b)] rises to the melting temperature and above up to the depth of $\sim 200 \text{ nm}$ (as a result of the electron-phonon energy exchange) and the pressure [Fig. 8(c)] reaches $\sim 1.5 \text{ GPa}$ [as a result of thermal expansion; see the blue crosses in Fig. 12(a)], the homogeneous melting does not occur. The reason is that the necessary overheating conditions needed for homogeneous melting do not hold long enough (50 ps, according to the criterion suggested in Appendix C; see Fig. 11, upper line). Since the homogeneous melting process is suppressed here, it cannot prevent the development and propagation of the compressive pressure wave [Fig. 8(c)]. The initial spatial pressure profile (at $t \approx 3 \text{ ps}$) has a peak near the front surface (because the laser energy absorption is stronger near this surface), but not at the surface itself, since the surface expansion allows the pressure to relax [cf. Fig. 8(a)]. The evolution of this pressure profile is essentially the same as in metallic targets [96,97]. It evolves as a superposition of a number of pressure sources propagating in two directions: to the front surface and to the rear surface. These waves sooner or later reach the free surfaces and are reflected with the opposite sign. Consequently, after two reflections from the front and rear free surfaces, the superposition of the wave sources gives the strongest positive pressure wave returning to the front surface [Fig. 8(c)].

As seen in Fig. 8(a), initially the heat expansion pushes the surface away, temporarily creating a 4 nm surface bump. After about $t \approx 100 \text{ ps}$ the shrinking of the material starts to prevail and the melting front is pushed back to the frontal surface. The material continues shrinking until $t \approx 200 \text{ ps}$, when the mentioned returning positive pressure wave starts to provide additional energy for the heterogeneous melting mechanism near the surface. The pressure wave pushes the surface back out of the material and assists the advance of the solid-liquid interface deeper into the bulk of the material, in accordance with Fig. 11. For higher fluences such effect is much more pronounced and is seen as peaks in the effective melting depths (see Sec. VC).

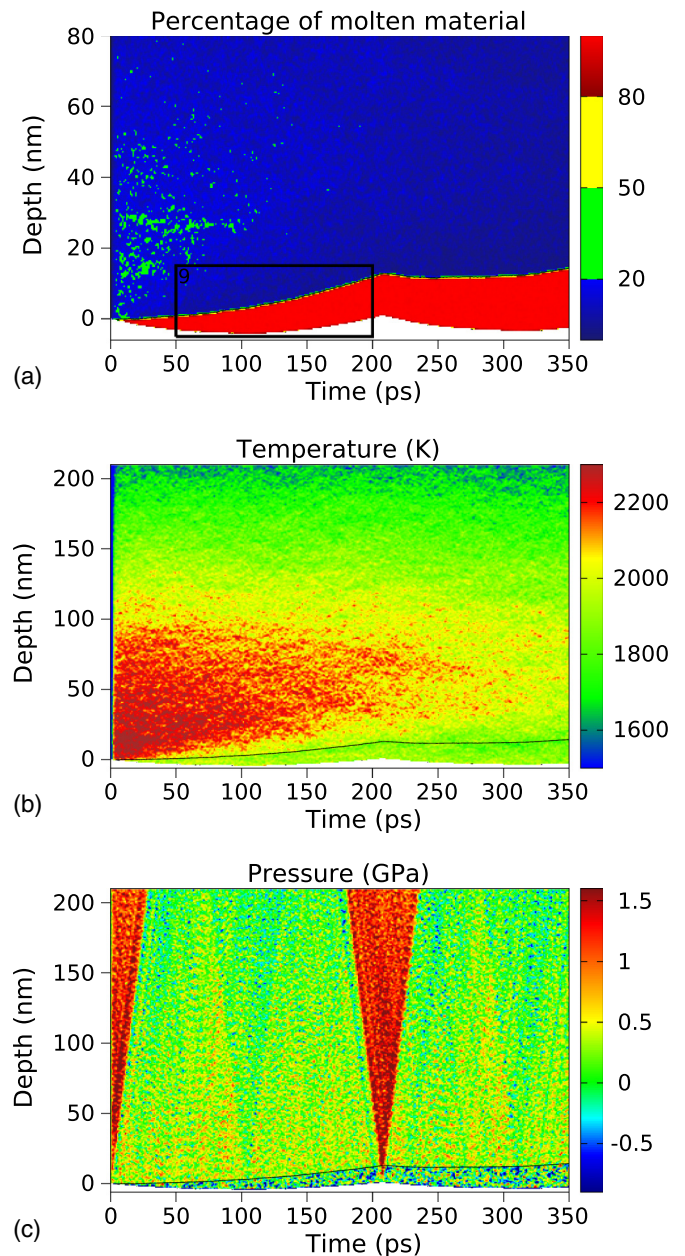


FIG. 8. (Color online) Contour plots of (a) percentage of molten material (according to the central symmetry parameter; see Appendix D), (b) atomic temperature, and (c) atomic pressure, obtained from the simulation of the 130 fs laser pulse focused on 800 nm silicon film at the absorbed fluence 0.161 J/cm^2 . The plot (a) is shown with different scale in order to provide a better view of the melting front. The black solid line is obtained from the plot (a) and shows the melting front assuming 50% of the material is molten. The rectangle on the plot (a) shows the position of the atomic configuration snapshots presented in Fig. 9.

C. Melting depth versus fluence

In this section, we discuss the effective melting depths for different laser fluences. The effective melting depths were

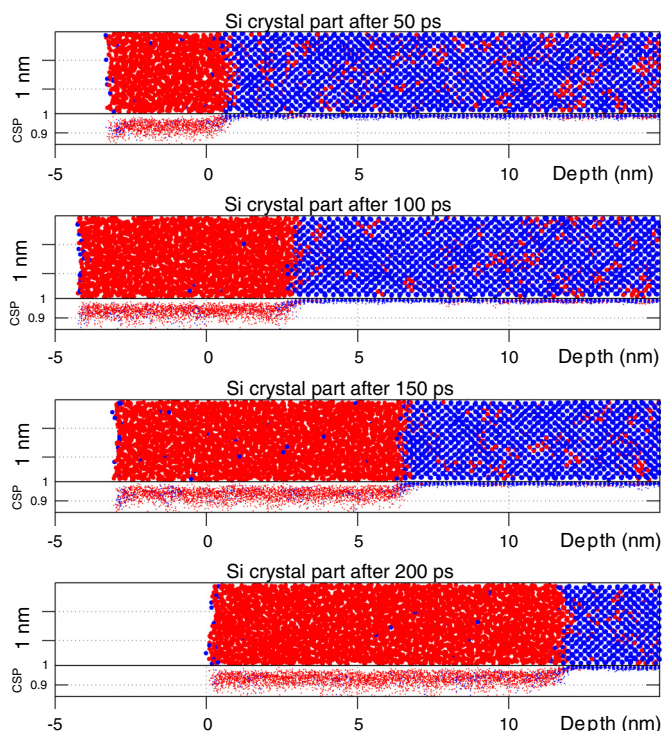


FIG. 9. (Color online) The snapshots of the simulation taken at different moments of time after the laser pulse. The laser pulse is directed from the left to the right. Only the front surface volume of the sample is shown. The original laser pulse was directed from the left to the right. This is the same simulation as in Fig. 8. This is the same style as in Fig. 5, but refers to rectangle 9 in Fig. 8.

found from the number of “molten atoms” (according to the central symmetry parameter; see Appendix D) at the certain moment of time by calculating the corresponding volume of liquid for this amount (referring to the atomic density under normal conditions). Cells with <50% of molten material were excluded in order to exclude unstable liquid nuclei, such as those in Fig. 7. We vary the total fluence, leaving all the other

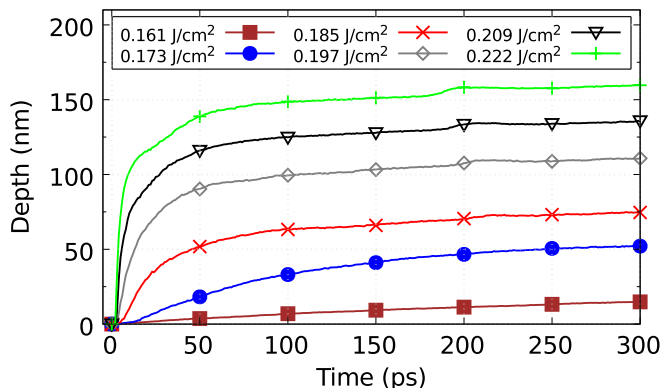


FIG. 10. (Color online) The effective melting depth depending on time for a set of the absorbed fluences: 0.161–0.222 J/cm². The lowest line corresponds to heterogeneous melting only.

parameters the same: 130 fs pulse duration, 800 nm laser wavelength, and 800 nm Si film thickness. The simulations were performed for the set of absorbed fluences from 0.114 to 0.221 J/cm² (corresponding to the incident fluences from 0.26 to 0.44 J/cm²). The temporal evolution of the effective melting depths is shown in Fig. 10. The model shows that for the absorbed fluences higher or equal to 0.173 J/cm², the quick initial increase in melting depth reflects that the homogeneous mechanism is dominant, whereas the following lower slope is connected to the heterogeneous process only [see Figs. 4(a) and 5–7]. In the case of lower fluences (Fig. 10; only 0.161 J/cm² is shown) only the heterogeneous melting occurs, which is confirmed by the snapshots in Fig. 9 and the contour plot in Fig. 8(a). The simulations under the same conditions, but performed for a 2000-nm-thick Si target confirm the threshold value of 0.173 J/cm². To our knowledge, this threshold was not mentioned in the literature before.

In Fig. 10, we observe humps in the effective melting depths for higher fluences at a time around ~200 ps after the pulse. As we already mentioned in the previous section, these sudden increases in the melting depth are connected to a compression wave, incoming to the front surface and assisting the propagation of the solid-liquid interface. The maximum effective melting depths were not reached for all our simulations. For the case of absorbed fluence of 0.209 J/cm², the maximum effective melting depth was reached in 850 ps after the laser pulse and its value was found to be 143 nm. This result differs from the corresponding experimental values of 60 nm (in the case of *n*-doped thick single-crystalline <111>-silicon [70]) and 55 nm (for 450-nm-thick undoped silicon wafers [69]). We mainly attribute it to the difference in the value of heat of fusion [see Fig. 12(b) and Table I], which is 31.2 kJ/mol for the Stillinger-Weber potential (as is confirmed by other MD simulations using the same potential [80,82]); yet its experimental value is 50.21 kJ/mol [98]. Nevertheless, the melting kinetics is described qualitatively accurate, because of the good representation of Clapeyron’s equation at our pressure conditions and other parameters of the material (Table I). Finally, the smallest absorbed fluence of 0.120 J/cm² (corresponding to the incident fluence of 0.27 J/cm²; not shown), at which the surface melting was detected, can be considered as the threshold value for the material modification and is in agreement with its experimental value [70] for our chosen value of a two-photon absorption coefficient.

VI. CONCLUSION

We have implemented an atomistic-continuum MD-*n*TTM model for silicon. First calculations showed its benefits as a powerful numerical tool to study short laser pulse interaction with freestanding Si films. The model is able to describe the melting kinetics with atomic resolution for fluences above the melting threshold. The approach provides microscopic insight into the processes occurring during and after the laser pulse. The energy conservation criterion fulfillment and the comparison of the obtained results with the ordinary

continuum model have confirmed the reliability of the model implementation.

The laser irradiation leads to two different melting regimes: heterogeneous and homogeneous. According to the simulations, at absorbed fluences below 0.173 J/cm^2 , the temperature and pressure—though providing the conditions for classical melting—are not high enough for the homogeneous melting. Therefore only heterogeneous melting occurs, starting from the surface, with a well-defined propagation front. Higher fluences induce the homogeneous melting, which takes the dominant character, and the resulting speed of melting front propagation becomes faster than the speed of sound. The temperature and pressure interrelation allowed one to explain these processes in detail and revealed the consequences of negative dependence of the equilibrium melting temperature on pressure. In first picoseconds, the strong heating rate results in the growth of compressive stresses, leading to positive pressure. In contrast to metals, positive pressure weakens the crystal stability against both heterogeneous and homogeneous melting, but is immediately consumed by the shrinkage of the material upon the melting process. This further results in the temporal relaxation of the material, undergone in the homogeneous melting process, and a number of liquid nuclei are incorporated into the yet crystal structure. The subsequent unloading (negative) pressure wave temporarily reinforces the stability of the residual crystalline structures. A heterogeneous process takes over the homogeneous one only after some tens of picoseconds and takes a much longer time.

For fluences higher or equal to the threshold value of 0.173 J/cm^2 , the effective melting depth rapidly increases in the first 10 ps after the laser pulse due to the quick homogeneous melting. Then the heterogeneous mechanism prevails and further melting proceeds at a much slower rate. At later stages, the incoming positive pressure waves from the rear side of the sample assist the heterogeneous melting resulting in the humps in the effective melting depth. Finally, after plateaus are reached, the material starts to recrystallize back to the diamond structure.

Therefore, from the obtained results, which reproduce the experimental data values up to the limit of the precision of the interatomic potential, and from the performed microscopic analysis of the melting process, we conclude that the suggested model can be used for a number of close insights of the laser-generated nonequilibrium processes in the Si material. Moreover, with additional efforts in the implementation of the parallel algorithm and three-dimensional heat conduction, simulations can cover temporal and spatial scales big enough to be directly attainable in the experiment for a direct comparison with the experiment. Finally, based on the model construction idea and the performed analysis, one can expect that, although the analyses in this work were done for silicon, the model in general should be applicable for other semiconductor solids with the appropriate interatomic potentials and the implemented properties of the electron-hole free-carrier's subsystem.

The melting kinetics of semiconductors under ultrashort laser irradiation is significantly different from that of metals with a fcc crystal structure due to the differences in crystallic structure and thermophysical properties. The close-packed

structure of metallic targets leads to low-pressure assisted melting, whereas in semiconductors low pressure reinforces the crystal stability against melting. In both, metals and semiconductors, liquid nuclei, formed inside the crystallic solid during homogeneous melting, reinforce the stability of the surrounding crystal. However, the reasons for that are different: In metals the expansion of the material during melting by 3%–5% leads to increased pressure, whereas semiconductor materials contract during melting by the order of 5%–7%. Particularly, this effect is strongly pronounced for silicon (the volume of melting is -7.5%), which results in its rough melting front. The effect of heat expansion is not so pronounced in semiconductors; therefore the laser-induced pressure is weaker than in metals. In metals, at the fluences around the melting threshold, the laser energy deposition depth can be estimated from the properties of material and is usually a constant not larger than a few tens of nanometers. Consequently, the areas of both homogeneous and heterogeneous melting are near to the surface, resulting in a well-defined solid-liquid interface despite possible homogeneous melting. In semiconductors, however, the laser energy deposition depth depends on the laser parameters and transient material state. This depth is much larger than the critical size of liquid nuclei, which is reflected in several nucleation regions remaining on different depths for a long time (sometimes until recrystallization).

The application of the model, however, is limited to fluences below those, at which changes in the interatomic potential due to electronic excitations become significant. Also, the one-dimensional model for the diffusion of free carriers and heat propagation, implemented in the current approach, is valid as long as the investigated target lateral size remains small as compared to the laser spot for particular experimental applications. Whenever this assumption is no longer valid, and the laser spot on the material surface becomes comparable with the size of the damaged region (ablation crater, generated surface feature), the suggested model must account for the 3D diffusion process in its continuum part. All listed limitations, however, are planned to be resolved in our future investigations.

ACKNOWLEDGMENTS

This work was supported by the Deutsche Forschungsgemeinschaft Grants No. IV 122/1, No. RE1141/14, and No. GA465/15-1. The authors acknowledge Nikita Medvedev and Anika Rämmer for the helpful discussions on the continuum model, Markus Nießen for the assistance in the development of the continuum solution scheme, and Nikita Shcheblanov for valuable comments on the implementation. The work was partly conducted at the Institute for Laser Technology (ILT), RWTH, Aachen, Germany, Department of Nonlinear Dynamics of Laser Processing (NLD), in the group of Prof. Wolfgang Schulz. The authors also acknowledge the support of the computational facilities of the University of Kassel and Technical University of Darmstadt. Additionally, the two anonymous reviewers are acknowledged for their helpful suggestions.

APPENDIX A: MODEL PARAMETERS

Name and symbol	Expression and units	References
Initial carrier density, n_0	10^{16} m^{-3}	[64]
Initial lattice and carrier temperature, T_0	300 K	
Lattice specific heat, C_a	$1.978 \times 10^6 + 3.54 \times 10^2 T_a - 3.68 \times 10^6 / T_a^2$, J/(m ³ K) (T_a in K)	[99]
Lattice thermal conductivity, k_a	$1.585 \times 10^5 T_a^{-1.23}$, W/(m·K) (T_a in K)	[99]
Carrier thermal conductivity, $k_e = k_h$	$-3.47 \times 10^{18} + 4.45 \times 10^{16} T_e$, eV/(s m K) (T_e in K)	[100]
Indirect band gap, E_g	$1.170 - 4.73 \times 10^{-4} \times T_a^2 / (T_a + 636) - 1.5 \times 10^{-10} \times n^{1/3}$ if $1.170 - 4.73 \times 10^{-4} \times T_a^2 / (T_a + 636) - 1.5 \times 10^{-10} \times n^{1/3} \geq 0$ and 0 otherwise, eV (T_a in K, n in m ⁻³)	[101,102]
Interband absorption (taken from 694 nm laser), α	$1.34 \times 10^5 \exp(T_a/427)$, m ⁻¹ (T_a in K)	[103]
Two-photon absorption, β	15 cm/GW	See Sec. II
Reflectivity, R	$0.329 + 5 \times 10^{-5} (T_a - 300)$ (T_a in K)	[74]
Auger recombination coefficient, γ	$3.8 \times 10^{-43} \text{ m}^6/\text{s}$	[104]
Impact ionization coefficient, δ	$3.6 \times 10^{10} \exp(-1.5 E_g / k_B T_e)$, s ⁻¹	[105]
Free-carrier absorption cross section, Θ	$2.91 \times 10^{-22} T_a / 300$, m ² (T_a in K)	[106]
Electron-phonon relaxation time, τ_{ep}	$0.5 \times 10^{-12} (1 + n / (2 \times 10^{27}))$, s (n in m ⁻³)	[100]
Electron effective mass, m_e^*	$0.36 m_e$	[107]
Hole effective mass, m_h^*	$0.81 m_e$	[107]
Mobility of electrons (taken at $T_e = 1000$ K), μ_e	$0.0085 \text{ m}^2/(\text{V}\cdot\text{s})$	[106]
Mobility of holes (taken at $T_e = 1000$ K), μ_h	$0.0019 \text{ m}^2/(\text{V}\cdot\text{s})$	[106]

APPENDIX B: ADDITIONAL EQUATIONS DEMANDED FOR THE CARRIER DESCRIPTION

In this Appendix we present the additional equations demanded to complement the system (1), (3), and (10). The full set of nonlinear differential equations therefore allows the description of laser irradiation of silicon in continuum. The derivation of the following expressions can be found elsewhere [55]. The electrons and holes are assumed to have two separate Fermi-Dirac distributions with shared temperature T_e , but different chemical potentials φ_e and φ_h , respectively [63]:

$$f_c(E) = \frac{1}{e^{\pm(E-\varphi_c)/k_B T_e} + 1}, \quad (\text{B1})$$

where subscript c stands as e for electrons and h for holes; the + sign is associated with electrons and the - sign with holes. The reduced chemical potentials are defined as follows:

$$\eta_e = \frac{\varphi_e - E_C}{k_B T_e} \quad \text{and} \quad \eta_h = \frac{E_V - \varphi_h}{k_B T_h}, \quad (\text{B2})$$

where E_C and E_V are the conduction and valence band energy levels, respectively, so the energy gap is $E_g = E_C - E_V$. The integration of the carrier distribution functions over the energy leads to the expressions for the carrier density (parabolic bands are assumed):

$$n = 2 \left[\frac{m_c^* k_B T_e}{2\pi \hbar^2} \right]^{3/2} F_{1/2}(\eta_c). \quad (\text{B3})$$

The Fermi-Dirac integral is defined as

$$F_\xi(\eta_c) = \frac{1}{\Gamma(\xi + 1)} \int_0^\infty \frac{x^\xi}{1 + \exp(x - \eta_c)} dx. \quad (\text{B4})$$

The electrons and holes are assumed to move together due to the Dember field preventing the charge separation. The carrier current is therefore

$$\vec{J} = -D \left\{ \nabla n + \frac{n}{k_B T_e} \left[H_{-1/2}^{1/2}(\eta_e) + H_{-1/2}^{1/2}(\eta_h) \right]^{-1} \nabla E_g + \frac{n}{T_e} \left[2 \frac{H_0^1(\eta_e) + H_0^1(\eta_h)}{H_{-1/2}^{1/2}(\eta_e) + H_{-1/2}^{1/2}(\eta_h)} - \frac{3}{2} \right] \nabla T_e \right\}, \quad (\text{B5})$$

where $H_\xi^\xi(\eta_c) \equiv F_\xi(\eta_c) / F_\xi(\eta_c)$ and the ambipolar diffusion coefficient is

$$D = \frac{k_B T_e}{q_e} \frac{\mu_e \mu_h H_{1/2}^0(\eta_e) H_{1/2}^0(\eta_h)}{\mu_e H_{1/2}^0(\eta_e) + \mu_h H_{1/2}^0(\eta_h)} \times \left[H_{-1/2}^{1/2}(\eta_e) + H_{-1/2}^{1/2}(\eta_h) \right]. \quad (\text{B6})$$

Ambipolar energy flow is the sum of diffusion and thermal energy currents inside the carrier subsystem and can be written as

$$\vec{W} = \left\{ E_g + 2k_B T_e \left[H_0^1(\eta_e) + H_0^1(\eta_h) \right] \right\} \vec{J} - (k_e + k_h) \nabla T_e. \quad (\text{B7})$$

APPENDIX C: PROPERTIES OF THE STILLINGER-WEBER SILICON

In order to have our atomistic-continuum MD- n TTM modeling results analyzed quantitatively, we must first find out the properties of the material represented with Stillinger-Weber potential for Si [49]. Among the properties that are of essential interest for us, one can point out the equilibrium melting temperature, volume of melting, enthalpy of fusion (latent heat of melting), linear expansion coefficient, and

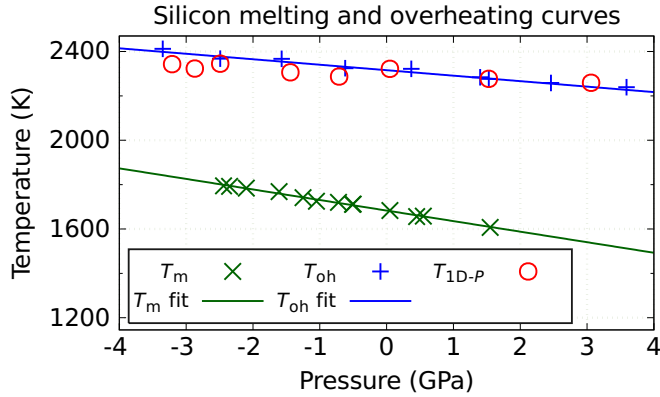


FIG. 11. (Color online) Equilibrium melting temperatures, T_m , and maximum overheating temperatures, T_{oh} and T_{1D-P} , for different pressure conditions. Green crosses are the results of liquid-crystal coexistence simulations with MD. Green solid line is the result of the corresponding fitting procedure. Blue pluses are the results of MD simulations on the maximum overheating temperature that the crystal can have without melting within at least 50 ps (see text). Blue solid line is the result of the corresponding fitting procedure. Red circles were calculated at conditions similar to blue pluses, except that the expansion and contraction of the sample were one dimensional.

heat capacity. In this Appendix we perform classical MD calculations in order to determine the material properties.

One of the most important parameters in our work, the equilibrium melting point, can be found from a sequence of liquid-crystal coexistence simulations. For this purpose a sample with $6 \times 6 \times 40$ lattice cells in X , Y , and Z dimensions, containing 11 500 atoms, was prepared partially molten at a certain pressure. Thereafter, the sample was equilibrated over a nanosecond so that the liquid and solid phases coexisted together at the stable pressure and temperature across the whole sample. This method excludes the presence of the nucleation barrier upon the phase transformation, and we therefore surely measure the equilibrium melting temperature at the given pressure. Performing a series of such simulations at different pressures, one can apply a linear fit to the obtained

data points according to Clapeyron's equation,

$$\left(\frac{dT}{dP}\right)_{T_m} = \frac{\Delta V_m}{\Delta S_m} = \frac{T_m \Delta V_m}{\Delta H_m}. \quad (C1)$$

This equation not only helps to define the equilibrium melting temperature for normal conditions, $T_m = 1683 \pm 2$ K ($P = 0$ GPa), but is also linked to other thermophysical properties such as entropy of fusion ΔS_m , volume of melting ΔV_m , and the latent heat of melting ΔH_m (enthalpy of fusion). From Fig. 11 one can see the relation between equilibrium melting temperature and pressure is different from that in metals [53,92]. Higher (lower) pressure assists (hinders) the melting process, therefore decreasing (increasing) the necessary temperature needed to melt the crystal. This result is in agreement with the silicon shrinkage during melting [see below, Fig. 12(a)].

Figure 11 further shows data at higher temperatures, which refer to the maximum possible overheating of the crystal before the onset of homogeneous nucleation of the liquid phase (blue pluses and blue solid line) for different pressure conditions. The corresponding simulations involved $12 \times 12 \times 12$ lattice cells with periodic boundary conditions. The crystal was considered stable in case liquid nuclei of the critical size do not appear within 50 ps after giving the velocities to the atoms. Note, that the choice of this time slightly influences the resulting maximum possible overheating temperature T_{oh} .

Similarly, we calculated the maximum possible overheating temperatures, T_{1D-P} , in the case of one-dimensional expansion/contraction of the solid (red circles in Fig. 11). The calculations show that, in contrast to metals [53], the presence of lateral crystal confinement for the realized heating conditions does not noticeably affect the maximum possible overheating of the crystal from that obtained at the homogeneous conditions. We therefore use T_{oh} in our analysis.

Other thermophysical properties such as volume of melting ΔV_m , latent heat of melting ΔH_m , linear expansion coefficient, and heat capacity of the represented material can be found from another sequence of constant pressure/constant temperature simulations. In these simulations for a sample with dimensions of $8 \times 8 \times 8$ lattice parameters, consisting of 4096 atoms, we can measure the volume and energy density as a function of temperature at $P = 0$ GPa, first for solid and then for

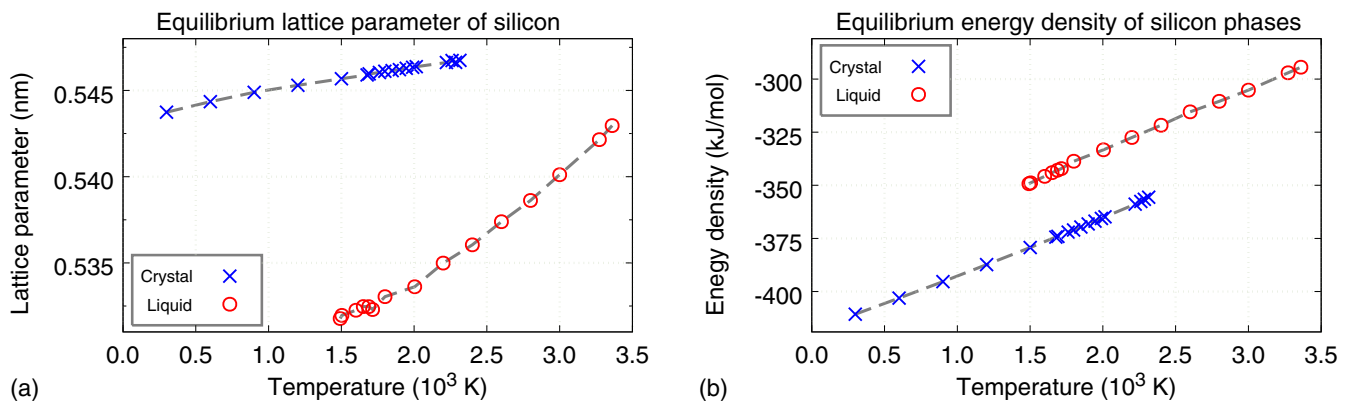


FIG. 12. (Color online) Thermophysical properties of the Stillinger-Weber silicon: (a) equilibrium lattice parameter for different temperatures at zero pressure; (b) equilibrium energy density for different temperatures at zero pressure. Blue crosses (showing solid phase) and red circles (showing liquid phase) are the results of MD simulations. Dashed lines are guides to the eye.

TABLE I. Comparison of the properties between the Stillinger-Weber silicon and experimental crystal.

Parameter	Calculated value	Experimental value	References
Lattice parameter (taken at 300 K)	0.543 74 nm	0.543 05–0.543 07 nm	[98,108]
Melting temperature	1683 ± 2 K	1687–1688 K	[98,108]
Volume shrinkage during melting	7.5%	7–9.6%	[108–111]
Enthalpy of fusion	31.2 kJ/mol	50.21 kJ/mol	[98]
Linear expansion coefficient (taken at 1000 K)	3.8×10^{-6} 1/K	4.3×10^{-6} 1/K	[98,112]
Heat capacity at constant pressure	$1.94 \times 10^6 + 2.32 \times 10^3 T_a$, J/(m ³ K)	See plotted data in the Reference	[113]
Heat capacity at constant volume	$2.00 \times 10^6 + 1.84 \times 10^2 T_a^2$, J/(m ³ K)(T_a in K)	$1.978 \times 10^6 + 3.54 \times 10^2 T_a - 3.68 \times 10^6 / T_a^2$, J/(m ³ K) (T_a in K)	[99]
Melting curve slope	–46.49 K/GPa	–58.7 K/GPa (near $P = 0$) or –60 K/GPa	[114], and references therein; [108]

liquid phases [Figs. 12(a) and 12(b)]. The jump between solid and liquid curves at the melting temperature corresponds to the volume of melting [Fig. 12(a)] and enthalpy of fusion [Fig. 12(b)]. Moreover, applying a linear fit to the lattice parameter as a function of temperature [Fig. 12(a)] and a fit of type $E = AT_a + BT_a^2/2$ for the energy as a function of temperature [Fig. 12(b)] we can take the derivative with respect to temperature and obtain the linear expansion coefficient and the heat capacity at zero pressure (see Table I).

The obtained results are collected in Table I and compared with their experimental values. We can see that the material properties represented by the Stillinger-Weber potential [49] for Si generally have a good match with the experimental data. We therefore analyze our results obtained with the MD- n TTM model quantitatively for the material represented with the given potential, and have some possibilities for their semiquantitative comparison with the experimental data.

APPENDIX D: PARAMETERS FOR DISTINGUISHING BETWEEN CRYSTAL AND LIQUID STRUCTURES

We use two different order parameters to distinguish between the crystal and liquid states of matter: local order parameter (LOP) [115] and modified central symmetry parameter (CSP), similar to that in Ref. [116]. We construct them for the diamond crystal structure and average their values over the nearest neighbors (first or second neighbor shell) to prevent large fluctuations.

To calculate the LOP for atom i we use the following definition:

$$\text{LOP}_i = \left| \frac{1}{6} \frac{1}{N_2} \sum_{j=1}^{N_2} \sum_{k=1}^6 \exp(i\vec{q}_k \vec{r}_{ij}) \right|^2. \quad (\text{D1})$$

Index j runs through all the neighbors of atom i inside the second neighbor shell ($N_2 = 12$ for ideal diamond structure).

The vectors $\{\vec{q}_k\}_{k=1}^6$ are defined as follows: $\vec{q}_1 = \frac{8\pi}{a} \{1; -1; 1\}$, $\vec{q}_2 = \frac{8\pi}{a} \{-1; 1; 1\}$, $\vec{q}_3 = \frac{8\pi}{a} \{1; 1; -1\}$, $\vec{q}_4 = \frac{8\pi}{a} \{0; 2; 2\}$, $\vec{q}_5 = \frac{8\pi}{a} \{2; 2; 0\}$, and $\vec{q}_6 = \frac{8\pi}{a} \{2; 0; 2\}$. $a = a(T)$ is the lattice parameter of the crystal depending on the atomic temperature [see Fig. 12(a)].

The CSP of atom i is calculated from the following expression:

$$\text{CSP}_i = 1 - \frac{[\sum_{j=1}^{N_1} (\vec{r}_{ij})]^2}{N_1 \sum_{j=1}^{N_1} \vec{r}_{ij}^2}, \quad (\text{D2})$$

where j runs over the nearest neighbors inside the first neighbor shell $r < \frac{1}{2}(\frac{\sqrt{3}}{4} + \frac{\sqrt{2}}{2})a$, $N_1 = 4$ for ideal diamond structure.

In the case of ideal crystal, the values of LOP and CSP are 1 for every atom and when the melting occurs, they quickly decay. Both LOP and CSP allow for a sharp distinction between the two phases of silicon with the chosen criteria (0.0155 for LOP and 0.9825 for CSP; please note that these values depend on the choice of the interatomic potential). CSP has somewhat higher precision (weaker noise) and does not depend on the crystal orientation. It also allows to distinct homogeneous recrystallization inside the liquid phase. For the discussions and interpretations, the CSP is used throughout the paper. We only apply LOP for coloring the graphs of CSP below the snapshots in Figs. 5–7 and 9.

The mentioned threshold values were found from the contour plot in Fig. 4(a). Initially the plot was calculated using LOP. We were decreasing the threshold for LOP starting from 1 until the first signs of (yellow) noise appear in the liquid (red) area in the plot. This means the noise became balanced between the crystal (blue) area and the liquid (red) area and is not greater than 20%. This led to the threshold value of 0.0155 for LOP. On the other hand, CSP does not show any noticeable noise in Fig. 4(a) even when its threshold is not well adjusted. We therefore found the latter from the best match of 50% melting fronts (black curves) between LOP and CSP variants of Fig. 4(a). As a result of using CSP with the found threshold value, the noise in Figs. 4(a), 5–7, 8(a), and 9–10 has been significantly decreased.

- [1] X. Liu, D. Du, and G. Mourou, *IEEE J. Quantum Electron.* **33**, 1706 (2002).
- [2] B. N. Chichkov, C. Momma, S. Nolte, F. von Alvensleben, and A. Tünnermann, *Appl. Phys. A* **63**, 109 (1996).
- [3] R. R. Gattass and E. Mazur, *Nat. Photonics* **2**, 219 (2008).
- [4] S. Y. Chou, C. Keimel, and J. Gu, *Nature (London)* **417**, 835 (2002).
- [5] R. Le Harzic, D. Dorr, D. Sauer, N. Neumeier, M. Epple, H. Zimmerman, and F. Stracke, *Phys. Proc.* **12**, 29 (2011).
- [6] E. Stratakis, A. Ranella, and C. Fotakis, *Biomicrofluidics* **5**, 013411 (2011).
- [7] A. Mathis, F. Courvoisier, L. Froehly, L. Furfaro, M. Jacquot, P. A. Lacourt, and J. M. Dudley, *Appl. Phys. Lett.* **101**, 071110 (2012).
- [8] M. K. Bhuyan, F. Courvoisier, P. A. Lacourt, M. Jacquot, R. Salut, L. Furfaro, and J. M. Dudley, *Appl. Phys. Lett.* **97**, 081102 (2010).
- [9] F. Courvoisier, P. A. Lacourt, M. Jacquot, M. K. Bhuyan, L. Furfaro, and J. M. Dudley, *Opt. Lett.* **34**, 3163 (2009).
- [10] T. H. R. Crawford, A. Borowiec, and H. K. Haugen, *Appl. Phys. A* **80**, 1717 (2005).
- [11] M. Toulemonde, S. Unamuno, R. Heddache, M. O. Lampert, M. Hage-Ali, and P. Siffert, *Appl. Phys. A* **36**, 31 (1985).
- [12] T. Grasser, T.-W. Tang, H. Kosina, and S. Selberherr, *Proc. IEEE* **91**, 251 (2003).
- [13] J. Bonse, S. M. Wiggins, and J. Solis, *J. Appl. Phys.* **96**, 2352 (2004).
- [14] L. V. Zhigilei, D. S. Ivanov, E. Leveugle, B. Sadigh, and E. M. Bringa, *Proc. SPIE* **5448**, 505 (2004).
- [15] B. Rethfeld, A. Kaiser, M. Vicanek, and G. Simon, *Phys. Rev. B* **65**, 214303 (2002).
- [16] N. S. Shcheblanov, T. J. Y. Derrien, and T. E. Itina, *AIP Conf. Proc.* **1464**, 79 (2012).
- [17] N. Medvedev and B. Rethfeld, *New J. Phys.* **12**, 073037 (2010).
- [18] N. Medvedev and B. Rethfeld, *Europhys. Lett.* **88**, 55001 (2009).
- [19] P. Stampfli and K. H. Bennemann, *Phys. Rev. B* **42**, 7163 (1990).
- [20] P. L. Silvestrelli, A. Alavi, M. Parrinello, and D. Frenkel, *Phys. Rev. Lett.* **77**, 3149 (1996).
- [21] E. S. Zijlstra, A. Kalitsov, T. Zier, and M. E. Garcia, *Adv. Mater.* **25**, 5605 (2013).
- [22] E. S. Zijlstra, A. Kalitsov, T. Zier, and M. E. Garcia, *Phys. Rev. X* **3**, 011005 (2013).
- [23] H. O. Jeschke, M. E. Garcia, M. Lenzner, J. Bonse, J. Krüger, and W. Kautek, *Appl. Surf. Sci.* **197**, 839 (2002).
- [24] V. I. Mazhukin, N. M. Nikiforova, and A. A. Samokhin, *Phys. Wave Phenom.* **15**, 81 (2007).
- [25] S. I. Anisimov, N. A. Inogamov, A. M. Oparin, B. Rethfeld, T. Yabe, M. Ogawa, and V. E. Fortov, *Appl. Phys. A* **69**, 617 (1999).
- [26] M. E. Povarnitsyn, T. E. Itina, M. Sentis, K. V. Khishchenko, and P. R. Levashov, *Phys. Rev. B* **75**, 235414 (2007).
- [27] S. I. Anisimov, B. L. Kapeliovich, and T. L. Perel'man, *Zh. Eksp. Teor. Fiz.* **66**, 776 (1974) [*JETP* **39**, 375 (1974)].
- [28] M. E. Povarnitsyn, T. E. Itina, K. V. Khishchenko, and P. R. Levashov, *Appl. Surf. Sci.* **253**, 6343 (2007).
- [29] G. L. Eesley, *Phys. Rev. B* **33**, 2144 (1986).
- [30] A. N. Smith and P. M. Norris, *Appl. Phys. Lett.* **78**, 1240 (2001).
- [31] J. L. Hostetler, A. N. Smith, and P. M. Norris, *Int. J. Thermophys.* **19**, 569 (1998).
- [32] H. E. Elsayed-Ali, T. Juhasz, G. O. Smith, and W. E. Bron, *Phys. Rev. B* **43**, 4488 (1991).
- [33] J. L. Hostetler, A. N. Smith, D. M. Czajkowsky, and P. M. Norris, *Appl. Opt.* **38**, 3614 (1999).
- [34] B. A. Remington, G. Bazan, J. Belak, E. Bringa, M. Caturla, J. D. Colvin, M. J. Edwards, S. G. Glendinning, D. S. Ivanov, B. Kad, D. H. Kalantar, M. Kumar, B. F. Lasinski, K. T. Lorenz, J. M. McNaney, D. D. Meyerhofer, M. A. Meyers, S. M. Pollane, D. Rowley, M. Schneider, J. S. Stolken, J. S. Wark, S. V. Weber, W. G. Wolfer, B. Yaakobi, and L. V. Zhigilei, *Metall. Mater. Trans. A* **35**, 2587 (2004).
- [35] Z. H. Jin and K. Lu, *Philos. Mag. Lett.* **78**, 29 (1998).
- [36] M. D. Kluge, J. R. Ray, and A. Rahman, *J. Chem. Phys.* **87**, 2336 (1987).
- [37] F. F. Abraham and J. Q. Broughton, *Phys. Rev. Lett.* **56**, 734 (1986).
- [38] H. Häkkinen and U. Landman, *Phys. Rev. Lett.* **71**, 1023 (1993).
- [39] F. F. Abraham, D. E. Schreiber, M. R. Mruzik, and G. M. Pound, *Phys. Rev. Lett.* **36**, 261 (1976).
- [40] J. A. Blink and W. G. Hoover, *Phys. Rev. A* **32**, 1027 (1985).
- [41] W. T. Ashurst and B. L. Holian, *Phys. Rev. E* **59**, 6742 (1999).
- [42] L. V. Zhigilei and B. J. Garrison, *Mater. Res. Soc. Symp. Proc.* **538**, 491 (1999).
- [43] J. I. Etcheverry and M. Mesaros, *Phys. Rev. B* **60**, 9430 (1999).
- [44] R. F. W. Herrmann, J. Gerlach, and E. E. B. Campbell, *Appl. Phys. A* **66**, 35 (1998).
- [45] E. Ohmura, I. Fukumoto, and I. Miyamoto, *Int. J. Jpn. Soc. Prec. Eng.* **32**, 248 (1998).
- [46] L. V. Zhigilei and B. J. Garrison, *J. Appl. Phys.* **88**, 1281 (2000).
- [47] L. V. Zhigilei, *Appl. Phys. A* **76**, 339 (2003).
- [48] N. A. Inogamov, V. V. Zhakhovskiy, Yu. V. Petrov, V. A. Khokhlov, S. I. Ashitkov, K. V. Khishchenko, K. P. Migdal, D. K. Ilnitsky, Yu. N. Emirov, P. S. Komarov, V. V. Shepelev, C. W. Miller, I. I. Oleynik, M. B. Agranat, A. V. Andriyash, S. I. Anisimov, and V. E. Fortov, *Contrib. Plasma Phys.* **53**, 796 (2013).
- [49] F. H. Stillinger and T. A. Weber, *Phys. Rev. B* **31**, 5262 (1985).
- [50] T. Kumagai, S. Izumi, S. Hara, and S. Sakai, *Comput. Mater. Sci.* **39**, 457 (2007).
- [51] D. S. Ivanov, A. I. Kuznetsov, V. P. Lipp, B. Rethfeld, B. N. Chichkov, M. E. Garcia, and W. Schulz, *Appl. Phys. A* **111**, 675 (2013).
- [52] B. S. Lee, S. Park, Y. K. Choi, and J. S. Lee, *J. Mech. Sci. Technol.* **25**, 449 (2011).
- [53] D. S. Ivanov and L. V. Zhigilei, *Phys. Rev. B* **68**, 064114 (2003).
- [54] D. P. Korfiatis, K.-A. Th. Thoma, and J. C. Vardaxoglou, *J. Phys. D: Appl. Phys.* **40**, 6803 (2007).
- [55] H. M. van Driel, *Phys. Rev. B* **35**, 8166 (1987).
- [56] T. J. Derrien, T. Sarnet, M. Sentis, and T. E. Itina, *J. Opt. Adv. Mater.* **12**, 610 (2010).
- [57] A. Rämmer, O. Osmani, and B. Rethfeld, *J. Appl. Phys.* **116**, 053508 (2014).
- [58] G. D. Tsibidis, M. Barberoglou, P. A. Loukakos, E. Stratakis, and C. Fotakis, *Phys. Rev. B* **86**, 115316 (2012).
- [59] Y. Gan and J. K. Chen, *Comput. Phys. Commun.* **183**, 278 (2012).

- [60] P. Lorazo, L. J. Lewis, and M. Meunier, *Phys. Rev. B* **73**, 134108 (2006).
- [61] L. Shokeen and P. K. Schelling, *Comput. Mater. Sci.* **67**, 316 (2013).
- [62] V. P. Lipp, D. S. Ivanov, B. Rethfeld, and M. E. Garcia, *J. Opt. Technol.* **81**, 254 (2014).
- [63] J. F. Young and H. M. van Driel, *Phys. Rev. B* **26**, 2147 (1982).
- [64] A. B. Sproul and M. A. Green, *J. Appl. Phys.* **70**, 846 (1991).
- [65] J. Crank and P. Nicolson, *Math. Proc. Cambridge Philosoph. Soc.* **43**, 50 (1947).
- [66] Tuncer Cebeci, *Convective Heat Transfer* (Springer, New York, 2002).
- [67] V. P. Lipp, D. S. Ivanov, B. Rethfeld, and M. E. Garcia (unpublished).
- [68] A. D. Bristow, N. Rotenberg, and H. M. Van Driel, *Appl. Phys. Lett.* **90**, 191104 (2007).
- [69] A. A. Ionin, S. I. Kudryashov, L. V. Seleznev, D. V. Sinitsyn, A. F. Bunkin, V. N. Lednev, and S. M. Pershin, *Zh. Eksp. Teor. Fiz.* **143**, 403 (2013) [*J. Exp. Theor. Phys.* **116**, 347 (2013)].
- [70] J. Bonse, *Appl. Phys. A: Mater. Sci. Process.* **84**, 63 (2006).
- [71] J. Bonse, S. Baudach, J. Krüger, W. Kautek, and M. Lenzner, *Appl. Phys. A* **74**, 19 (2002).
- [72] J. Bonse, K.-W. Brzezinka, and A. J. Meixner, *Appl. Surf. Sci.* **221**, 215 (2004).
- [73] E. J. Yoffa, *Phys. Rev. B* **21**, 2415 (1980).
- [74] G. E. Jellison and F. A. Modine, *Phys. Rev. B* **27**, 7466 (1983).
- [75] J. K. Chen, D. Y. Tzou, and J. E. Beraun, *Int. J. Heat Mass Transfer* **48**, 501 (2005).
- [76] M. P. Allen and D. J. Tildesley, *Computer Simulation of Liquids* (Oxford University Press, New York, 1987).
- [77] J. Tersoff, *Phys. Rev. B* **38**, 9902 (1988).
- [78] S. J. Cook and P. Clancy, *Phys. Rev. B* **47**, 7686 (1993).
- [79] M. I. Baskes, *Phys. Rev. B* **46**, 2727 (1992).
- [80] S. Ryu and W. Cai, *Modell. Simul. Mater. Sci. Eng.* **16**, 085005 (2008).
- [81] V. S. Dozhikov, A. Yu. Basharin, and P. R. Levashov, *J. Chem. Phys.* **137**, 054502 (2012).
- [82] M. H. Grabow, G. H. Gilmer, and A. F. Bakker, *MRS Online Proc. Libr.* **141**, 349 (1988).
- [83] S. G. Volz and G. Chen, *Phys. Rev. B* **61**, 2651 (2000).
- [84] C. A. da Cruz, K. Termentzidis, P. Chantrenne, and X. Kleber, *J. Appl. Phys.* **110**, 034309 (2011).
- [85] H. Balamane, T. Halicioglu, and W. A. Tiller, *Phys. Rev. B* **46**, 2250 (1992).
- [86] J. Q. Broughton and X. P. Li, *Phys. Rev. B* **35**, 9120 (1987).
- [87] A. Rouse, C. Rischel, S. Fourmaux, I. Uschmann, S. Sebban, G. Grillon, Ph. Balcou, E. Förster, J. P. Geindre, P. Audebert, J. C. Gauthier, and D. Hulin, *Nature (London)* **410**, 65 (2001).
- [88] M. Head-Gordon and J. C. Tully, *J. Chem. Phys.* **103**, 10137 (1995).
- [89] D. M. Duffy and A. M. Ruthersford, *J. Phys.: Condens. Matter* **19**, 016207 (2007).
- [90] E. Zarkadoula, S. Daraszewicz, D. M. Duffy, M. Seaton, I. T. Todorov, K. Nordlund, M. T. Dove, and K. Trachenko, *J. Phys.: Condens. Matter* **26**, 085401 (2014).
- [91] L. V. Zhigilei and D. S. Ivanov, *Appl. Surf. Sci.* **248**, 433 (2005).
- [92] D. Errandonea, *J. Appl. Phys.* **108**, 033517 (2010).
- [93] B. Rethfeld, K. Sokolowski-Tinten, D. von der Linde, and S. I. Anisimov, *Phys. Rev. B* **65**, 092103 (2002).
- [94] L. V. Zhigilei, Z. Lin, and D. S. Ivanov, *J. Phys. Chem. C* **113**, 11892 (2009).
- [95] *Smithells Metals Reference Book*, edited by W. F. Gale and T. C. Totemeier (Butterworth-Heinemann, Oxford, 2003).
- [96] D. S. Ivanov and L. V. Zhigilei, *Phys. Rev. Lett.* **91**, 105701 (2003).
- [97] E. Leveugle, D. S. Ivanov, and L. V. Zhigilei, *Appl. Phys. A* **79**, 1643 (2004).
- [98] D. R. Lide (ed.), *CRC Handbook of Chemistry and Physics*, 90th ed. (CRC Press/Taylor and Francis, Boca Raton, FL, 2010).
- [99] R. F. Wood and G. E. Giles, *Phys. Rev. B* **23**, 2923 (1981).
- [100] D. Agassi, *J. Appl. Phys.* **55**, 4376 (1984).
- [101] C. D. Thurmond, *J. Electrochem. Soc.* **122**, 1133 (1975).
- [102] R. Vankemmel, W. Schoenmaker, and K. De Meyer, *Solid State Electron.* **36**, 1379 (1993).
- [103] G. E. Jellison and F. A. Modine, *Appl. Phys. Lett.* **41**, 180 (1982).
- [104] J. Dwiezor and W. Schmid, *Appl. Phys. Lett.* **31**, 346 (1977).
- [105] J. Geist and W. K. Gladden, *Phys. Rev. B* **27**, 4833 (1983).
- [106] J. R. Meyer, M. R. Kruer, and F. J. Bartoli, *J. Appl. Phys.* **51**, 5513 (1980).
- [107] Ioffe Physical Technical Institute, Electronic Archive “New Semiconductor Materials. Characteristics and Properties”, <http://www.ioffe.rssi.ru/SVA/NSM/Semicond/Si/index.html>.
- [108] E. Yu. Tonkov, *Phase Transformations of Elements Under High Pressure* (CRC Press, Boca Raton, FL, 2005).
- [109] V. M. Glazov and O. D. Shchelikov, *High Temp.* **38**, 405 (2000).
- [110] Qi Zhang, Qikai Li, and Mo Li, *J. Chem. Phys.* **138**, 044504 (2013).
- [111] R. A. Logan and W. L. Bond, *J. Appl. Phys.* **30**, 3 (1959).
- [112] H. Watanabe, N. Yamada, and M. Okaji, *Int. J. Thermophys.* **25**, 221 (2004).
- [113] A. S. Okhotin, A. S. Pushkarskii, and V. V. Gorbachev, *Thermophysical Properties of Semiconductors* (“Atom” Publishing House, Moscow, 1972) (in Russian), <http://www.mitht.ru/e-library/fund?id=12654>.
- [114] C. C. Yang, J. C. Li, and Q. Jiang, *Solid State Commun.* **129**, 437 (2004).
- [115] J. R. Morris and X. Song, *J. Chem. Phys.* **116**, 9352 (2002).
- [116] P. J. Steinhardt, D. R. Nelson, and M. Ronchetti, *Phys. Rev. B* **28**, 784 (1983).